Land Surface Temperature Reconstruction Under Long-Term Cloudy-Sky Conditions at 250 m Spatial Resolution: Case Study of Vinschgau/Venosta Valley in the European Alps

Paulina Bartkowiak ⓘ, *Student Member, IEEE*, Mariapina Castelli, Alice Crespi, Georg Niedrist,
Damiano Zanotelli ⓘ, Roberto Colombo ⓘ, and Claudia Notarnicola ⓘ, *Member, IEEE*

Abstract—In this article, we present a new concept for predicting satellite-derived land surface temperature (LST) under cloudy skies over vegetated areas in the Alps. Although many different reconstruction methods have been developed, they require rarely available inputs, or they restore missing pixels from clear-sky observations with low spatial resolution (1–5 km), which makes them unreliable in heterogenous ecosystems. Given these limitations, we propose a station-based procedure to predict cloud-covered grids from 1-km Terra MODIS LST at 250 m spatial resolution. First, we explored correlations between ground-measured LST and air temperature in conjunction with other geo-biophysical variables under cloudy-sky conditions derived from ESRA clear-sky radiation model. Considering a high site dependency driven by different landcovers, in-situ data were aggregated into three groups (forest, permanent crops, grassland) and then, models were established. Next, the regressions were applied to 250-m gridded predictors to estimate cloud-covered LST pixels for six Terra MODIS LST images in 2014. While for permanent crops and forest group linear modelling was the most efficient, neural networks achieved the best performance for grasslands. The reconstructions showed reasonable LST distribution considering landscape heterogeneity of the region. The results were validated against timeseries of ground-measured LST in 2014. The models achieved reliable performance with an average R^2 of 0.84 and root-mean-square error of 2.12 °C. Despite some limitations, mainly due to diversified character of cloudy-sky conditions and high heterogeneity of gridded predictors, the method can effectively reconstruct overcast MODIS data at subpixel level, which shows great potential for producing cloud-free LSTs in complex ecosystems.

Index Terms—Cloudy-sky conditions, land surface temperature, machine learning, reconstruction.

I. INTRODUCTION

EARTH'S skin temperature is a fundamental property regulating the exchange of water and energy between land and the atmosphere. Thus, it influences water and surface energy budget that is needed to estimate the impacts of climate change on water cycling, landcover, and to examine water anomalies in vegetation through evapotranspiration modeling [1]–[3]. Moreover, it allows monitoring vegetation conditions and studying climate change and impacts of extreme events on vegetation. As a result, land surface temperature (LST) is required as a baseline information for many environmental applications, such as management of water resources, climate change studies, sustainable agricultural production, drought predictions, and also land degradation monitoring [4]–[6].

Since the global network of meteorological stations is sparse, especially with regards to radiometers monitoring thermal infrared radiation, and LSTs vary over short distances, thermal remote sensing has shown large potential due to its spatial coverage and accessibility [7]–[9]. The rapid development of spaceborne thermal infrared (TIR) instruments followed by robust LST retrieval methods has allowed monitoring spatially and temporally continuous LSTs at different scales [10]. In particular, MODIS instrument has been frequently used due to its short repeat cycle (four times per day), global coverage and long-term image collection (since 2000) [11]. MODIS LST product has been applied in multiple research fields, including urban heat island assessment [12]–[15], drought detection [16]–[19], agricultural management [7], [20], [21], and energy and water balance modelling [22]–[25].

Although MODIS LST maps have been commonly used in many studies, TIR sensors are prone to overcast conditions. TIR instruments cannot acquire spatial information beneath clouds

Paulina Bartkowiak is with the Institute for Earth Observation, Eurac Research, 39100 Bozen-Bolzano, Italy, and also with the Department of Earth and Environmental Sciences, University of Milano-Bicocca, I-20126 Milan, Italy (e-mail: paulina.bartkowiak@eurac.edu).

Mariapina Castelli, Alice Crespi, and Claudia Notarnicola are with the Institute for Earth Observation, Eurac Research, 39100 Bozen-Bolzano, Italy (e-mail: mariapina.castelli@eurac.edu; alice.crespi@eurac.edu; claudia.notarnicola@eurac.edu).

Georg Niedrist is with the Institute for Alpine Environment, Eurac Research, 39100 Bozen-Bolzano, Italy (e-mail: georg.niedrist@eurac.edu).

Damiano Zanotelli is with the Faculty of Science and Technology, Free University of Bozen-Bolzano, 39100 Bozen-Bolzano, Italy (e-mail: damiano.zanotelli@unibz.it).

Roberto Colombo is with the Department of Earth and Environmental Sciences, University of Milano-Bicocca, I-20126 Milan, Italy (e-mail: roberto.colombo@unimib.it).

Digital Object Identifier 10.1109/JSTARS.2022.3147356

that translates to invalid LST images with a strong impact on high-frequency cloud-contaminated areas [26]. According to Jin [27], cloudy skies "represent more than half of the actual day-to-day weather conditions" resulting in minimum 50% blank LST scenes from TIR data. If we focus on mountain regions, cloud cover is much more common and intense, which causes substantial gaps in LST images in space and time. Therefore, spatially, and temporally continuous LST information is of great importance and its complete creation is an urgent issue among the scientific community.

Methods for reconstructing land surface temperature at cloud-covered pixels have been well demonstrated in many research studies. In general, they can be aggregated into empirical and physical-based categories. The methods of the physical-driven group rely on the assumption that cloud-covered pixels differ from LST values under clear-sky conditions. Prediction of these temperatures requires knowledge about physical relationship between targets and their adjacent cloud-free pixels. Jin [27] developed a "neighboring-pixel" (NP) method that uses surface energy balance (SEB) to recover invalid values from their spatially (100–300 km) or temporally ($\leq$ two days) neighboring cloud-free pixels. Due to temporal limitations of the NP method, Lu *et al.* [28] proposed an enhanced solution based on geostationary satellite data from the MSG SEVIRI radiometer with shorter repeat cycle with respect to polar-orbiting satellites. Later, Yu *et al.* [29] adapted the NP by exploiting the spatiotemporal domain offered by MODIS LST product. Because of the physical complexity of this method and scarcity of the station-based inputs, such as wind speed and latent heat flux, some new approaches were proposed. Using MSG satellite data, Zhang *et al.* [30] predicted cloud-covered LST from a simplified heat transfer formula with the reduced number of station-based parameters. Next, Zeng *et al.* [31] developed a multisource approach that estimates invalid pixels from cloud-free MODIS LST in reference to normalized difference vegetation index (NDVI) and then applies a SEB-based factor to obtain values under cloudy skies. After that, Yang *et al.* [32] simplified the NP and showed that applying only solar radiation as the auxiliary feature can well estimate missing MODIS LST for areas significantly covered by clouds. Meanwhile, Martins *et al.* [33] developed an operational "all-weather land surface temperature" product based on the clear-sky 3-km MSG SEVIRI scenes and LST data under cloudy conditions derived from the surface energy balance model through the LSA-SAF ET v2 algorithm. In addition to the SEB-based strategies, Fu *et al.* [34] proposed a novel reconstruction method for urban areas by exploiting relationship between LSTs from the physical-based WRF/UCM system and clear-sky MODIS data using random forest algorithm. However, the performance of these approaches depends on the complexity of the study area or the availability of clear-sky LST, which makes it difficult to implement in ecosystems with extremely high variability with regard to weather conditions, altitude, soil, and landcover. Apart from the physical-based methods, cloud-covered LSTs can be recovered by data fusion approach by combining data from different resources. Many studies showed that TIR-based land surface temperature can be predicted by its integration with temporally adjacent

images from passive microwave instruments that are capable of penetrating clouds [35]–[39]. Furthermore, Long *et al.* [40] combined clear-sky MODIS data with 7-km LST dataset from China Land Data Assimilation System using ESTARFM algorithm and obtained all-weather 1-km MODIS-like scenes with root-mean-square error (RMSE) yielding from 2.77 K to 3.96 K. Similarly, the performances of these methods have limitations in terms of low spatial resolution of the cloud-free inputs.

The second category for LST reconstruction belongs to empirical methods and treats pixels obscured by clouds as those under clear skies. A widely used technique of this group is geostatistical interpolation that exploits similarities from neighboring clear-sky pixels in spatial, temporal, and spatiotemporal domain [41]–[45]. Furthermore, Crosson *et al.* [46] implemented multisensor approach to predict Aqua MODIS LST from clear-sky Terra MODIS LST and increased daytime and nighttime data availability of Aqua product by 24% and 30%, respectively. In addition, Wang *et al.* [47] approximated cloudy LSTs for Terra MODIS and Landsat-8 TIRS by spatiotemporal fusion of clear-sky multitemporal MODIS LST composites (MOD11A2) and synthetic surface temperatures with "solar-cloud-satellite geometry" derived from MODIS cloud and geolocation products (MOD06, MOD03) and Landsat-8 data. The empirical approaches, similarly to physical-based methods, rely on the availability of time-coincident cloud-free LSTs and input accuracies, which decreases their spatial prediction performance. To overcome this limitation, Ke *et al.* [48] exploited the relationship between MODIS LST and other environmental variables using regression kriging technique. As shown by Fan *et al.* [49], incorporation of NDVI, soil moisture and landcover information in conjunction with artificial neural networks and regression tree modeling allowed predicting missing LST with RMSEs ranging from 1.32 K to 1.66 K. Given the high capabilities of artificial intelligence (AI), new machine learning-based approaches have been recently developed. For example, Wu *et al.* [50] combined a convolutional neural network (CNN) with spatiotemporal information offered by geostationary instruments and obtained a prediction error of approximately 1 K for images with 70% cloud-contaminated pixels. Meanwhile, Zhao and Duan [51] proposed a random forest approach to predict MODIS LST by combining multisource remote sensing predictors with solar radiation to represent a cloud cover impact on missing LST pixels. However, the accuracies of these approaches are still highly influenced by the availability of clear pixels and low spatial resolution of satellite data that limits their application to a relatively homogenous terrain.

To address these limitations, in this article, we concentrate on the development of a new method to reconstruct cloud-covered 1-km MODIS LST at 250 m spatial resolution over vegetated areas in the European Alps. Considering high spatio-temporal dynamics of surface temperatures, we propose a new approach that integrates data-driven modeling with physical-based assumptions to detect long-term cloudy-sky conditions at subpixel level with respect to the 1-km original MODIS LST. The proposed method exploits relationship between ground-based LST and commonly accessible input parameters under
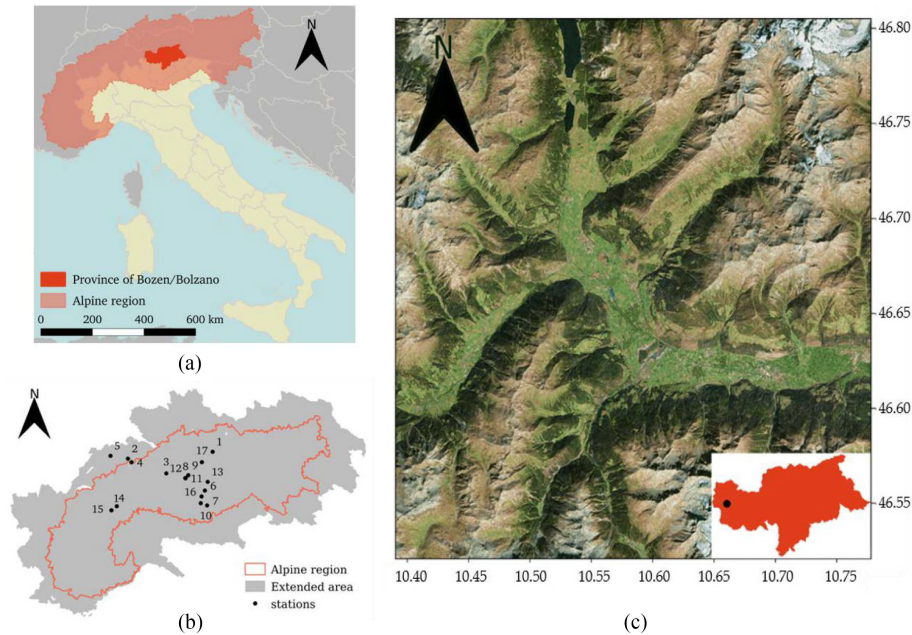
Fig. 1. Overview of the study case. (a) Location of Province of Bozen/Bolzano. (b) Positions of the stations utilized in the ground-based LST modeling. Some stations were situated outside the official border of the Alps (in red).[1] Since they were located in areas with similar climatic conditions, they were included in the modeling. (c) Satellite image of the experimental area for the LST reconstruction in Vinschgau/Venosta Valley obtained from the Express Kosmosnimki service.[2]

cloudy-sky conditions, like air temperature (TA), downwelling solar radiation (SW_{in}), surface albedo (α), and leaf area index (LAI), for spatial reconstructions of cloud-covered MODIS LST data. To our best knowledge, gap-filling from station-based models in conjunction with a physical-based approach to obtain *in situ* observations under cloudy skies has never been performed before. We analyze the prediction performance of the developed method based on different machine learning algorithms to reconstruct missing MODIS LST values. Through the application of different modelling scenarios, it is feasible to investigate in which way algorithms and predictors can explain LST variability within diversified mountain ecosystems. Due to limitations of MODIS LST pixel size, our concept predicts invalid grids at 250 m spatial resolution in order to minimize the impact of topography and landscape heterogeneity of the study area. Additionally, the reconstructed maps implemented in this article will be combined with 250-m downscaled Terra MODIS LST [52] for further energy balance modeling of evapotranspiration with relevant implications on water assessment in the Alps.

II. DATA AND METHODOLOGY

A. Study Site

Our area of interest is an approximately 520-km^2 region of Vinschgau/Venosta Valley in the northwestern part of the Province of Bozen/Bolzano, located in the Eastern Italian Alps (see Fig. 1(a)–(c)). The area is predominantly mountainous with elevation ranging from about 700 m to 3740 m a.s.l. Alpine orography has a significant impact on the structure of the landscape with highly patched landcovers over the region.

The area is mainly dominated by forests, grasslands, and apple orchards. Because of the insular location of the valley and the sheltering effect of the neighboring mountain ridges, the climate is warmer and drier than in other parts of the Alps, which translates to higher evaporation [53]. This results in unfavorable effects for vegetation, especially for grasslands and agricultural crops with higher demand for water. Considering the particular climatic conditions and agriculture-oriented land management, this region would particularly benefit of accurate reconstructed LST maps for monitoring vegetation conditions and water availability.

Land surface temperature reconstruction was performed based on year-round station records from the Fluxnet network and other stations located over different vegetated ecosystems in the Alps [see Fig. 1(a) and (b)] [54]. Eddy covariance data outside the Fluxnet network were processed in the framework of the project CYCLAMEN (https://www.eurac.edu/).

B. Input Data

1) Ground Measurements: Since this article is intended for vegetation analyses over the Alps, *in situ* measurements were collected at 17 meteorological sites distributed over different ecosystems, during the phenological cycle, between April and October (see Table I). The station loggers had unique time-series measurements recorded between 2002 and 2019 with 15- and 30-min intervals. As Table I shows, 10 sites are located above 1000 m and covered by grassland or forest, while the remaining seven stations lie in agricultural areas at altitudes below 1000 m.

In this article, we exploited ground-based upwelling and downwelling longwave radiation (LW_{in}, LW_{out}) to retrieve land surface temperature for each station record (see Table II) [55], [56]. In order to keep time consistency with MODIS LST data,

---

[1][Online]. Available: http://www.eurac.edu/
[2][Online]. Available: http://kosmosnimki.ru/

TABLE I
METEOROLOGICAL STATIONS UTILIZED IN THE LST MODELING

Model	LULC	Group	Station	Fluxnet site	Altitude [m a.s.l.]	Time span	
(1)	Grassland	Grassland	Rotholz (1)	AT-Rtz	523	2008	2012
			Chamau (2)	CH-Cha	393	2006	2012
			Früebüel (4)	CH-Fru	982	2006	2012
			Neustift (17)	AT-Neu	970	2002	2012
			Oensingen (5)	CH-Oe1	452	2003	2008
			Monte Bondone (10)	IT-MBo	1553	2003	2013
			Mazia 1 (11)	-	1450	2014	2017
			Mazia 2 (12)	-	1550	2014	2017
			Mazia 3 (8)	-	1909	2019	2019
			Mazia 4 (9)	-	2688	2016	2019
			Torgnon 1 (14)	(IT-Tor)	2160	2008	2017
(2)	Apple Orchard Vineyard	Permanent crops	Caldaro (6)	-	240	2014	2015
			Valle dell'Adige (16)	IT-VdA	206	2008	2010
(3)	Evergreen needleleaf forest Deciduous needleleaf forest	Forest	Lavarone (7)	IT-Lav	1349	2003	2014
			Davos (3)	CH-Dav	1639	2006	2011
			Renon (13)	IT-Ren	1730	2004	2013
			Torgnon 2 (15)	IT-TrF	2091	2010	2016

*Numbers in parentheses in the forth column refer to station locations presented in Fig. 1(b).

TABLE II
STATION-BASED PARAMETERS FROM YEAR-ROUND OBSERVATIONS AND THEIR CORRESPONDING VARIABLES USED FOR LST MODELING

Source data	Variable	Short description
Outgoing and incoming longwave radiation	Land Surface Temperature [°C] $\left(\dfrac{LW_{out} - (1-\varepsilon)LW_{in}}{\sigma\varepsilon}\right)^{1/4}$	LST formula based on Stefan–Boltzmann law [55], where σ is the Stefan–Boltzmann constant, ε is the surface emissivity from M*D21A1D [57], and LW_{out}/LW_{in} is the outgoing/incoming longwave radiation retrieved from ground observations
Air temperature	Mean air temperature (TA_{mean}) [°C] Maximum air temperature (TA_{max}) [°C]	daily mean and maximum air temperature derived from in-situ data
Solar radiation	Daily incoming shortwave radiation (SW_{in}) [MJ m^{-2}day^{-1}]	daily cumulative SW_{in} retrieved from ground observations
Surface albedo	Vegetation parameter [-] $\dfrac{\log(z_0)}{\alpha}$	aerodynamic roughness length (z_0) and albedo (α) to describe canopy structure

longwave radiation was extracted that corresponded to the local MODIS observing time. To compute surface temperature, we calculated broadband surface emissivity from daily MODIS land surface emissivity (LSE) product (M*D21A1D Collection 6) [57], as described by Wang *et al.* [58]. M*D21A1D was selected rather than daily M*D11A1, as it was created using physical-based temperature emissivity separation algorithm instead of simplified landcover-derived emissivity retrieval [59]. Even though 90-m ASTER LSE product offers finer spatial resolution, its small spatial extent, and 16-day repeat cycle in conjunction with frequent cloudiness over the study area hampered its practical applicability.

Due to strong correlation of LST with air temperature (TA) and availability of daily TA maps (see Section II-B2), observations of daily mean and maximum air temperature (TA_{mean}, TA_{max}) were computed from the *in situ* measurements and considered as the baseline input for modeling [60], [61]. In mountain regions with heterogenous landscape, such as the Alps, LST is influenced by complex interactions between land and atmosphere, solar energy, topography, soil moisture, and landcover. In this context, we exploited auxiliary ground-based biophysical parameters that may explain spatial variation in LST

over the study area (see Table II). In addition to TA_{mean} and TA_{max}, we incorporated diurnal incoming shortwave radiation (SW_{in}) that regulates ground heating process with an important impact on land-atmosphere energetics [53]. Owing to the energy fluxes between atmosphere and various vegetated landcovers, we combined surface albedo (α) with aerodynamic surface roughness (z_0, as in Table II) assigned for each landcover group separately as a complementary biophysical predictor for LST modeling [61]–[63].

All collected measurements were averaged to hourly resolution corresponding to MODIS acquisition time and they were inspected for the presence of outliers, including detection of inconsistent minimum and maximum station records and unusual temporal variations. Additionally, we performed a specific quality control procedure for solar radiation data by applying physical thresholds and step tests, specially adapted to Alpine conditions [64]. After these checks, the ground-based predictors for the LST modelling were computed (see Table II).

2) Gridded Data: Gridded variables were generated for reconstructing cloud-contaminated 1-km MODIS LST pixels at subpixel (250 m) spatial resolution from the fitted models (see Table III) .

TABLE III
GRIDDED DATASETS USED IN THIS ARTICLE

Source data	Variable	Pixel size	Short description
Prediction of missing MODIS LST pixels			
In-situ weather station records	Daily grids of: Mean air temperature (TA_{mean}) [°C] Maximum air temperature (TA_{max}) [°C]	250 m	Maps derived from daily station observations through a spatial interpolation scheme
MSG/SEVIRI DSSF	Downscaled daily incoming shortwave radiation maps [MJ m^{-2}day^{-1}]	250 m	Downscaled MSG downwelling surface shortwave flux (DSSF) through RK interpolation
MCD43A3	Vegetation parameter [-] $\dfrac{\log(z_0)}{\alpha}$	500 m	Relationship between aerodynamic roughness length (z_0) and albedo (α) from MCD43A3 composites
MCD15A3H[1]	$f_1(z_0, LAI)$: $z_0 \cdot (h)^{-1}{}_{CM88}$ [-] $f_2(z_0, LAI)$: $z_0 \cdot (h)^{-1}{}_{SD00}$ [-]	500 m	Vegetation structure parametrization (f_1, f_2) with roughness length (z_0) and leaf area index (LAI) obtained from MCD15A3H. Parameter h refers to vegetation height, and CM88 and SD00 subscripts indicate adopted formulas of Choudhury & Monteith [68] and Schaudt & Dickinson [69], respectively
MOD21A1D[2] MYD21A1D[2]	Emissivity bands: 29,31,32 [-]	1000 m	Daily emissivity maps from M*D21A1D composites for station-based LST retrieval (see Table II for more details)
Determination of spatial applicability of the reconstructed LST maps			
MOD11A1	Cloud cover [-]	1000 m	Cloud cover from daily Terra MODIS LST product to identify cloudy pixels
Snow Cover Area (SCA)	Snow cover [-]	250 m	Daily snow maps based on Terra and Aqua MODIS Reflectance for masking areas covered by snow
LISS 2013 - Land Information System South Tyrol	Vegetation mask [-]	-	Vegetation mask for identification of homogeneous landcovers within 250-m pixels (80% threshold of homogeneity)
MOD13Q1	Enhanced Vegetation Index (EVI) [-]	250 m	EVI grids from Terra MODIS Vegetation Indices product to delineate pixel-wise areas of applicability for the models

[1]Data used for both the station-based modelling and the reconstruction of missing MODIS LST pixels; [2]Data used for station-based LST retrieval.
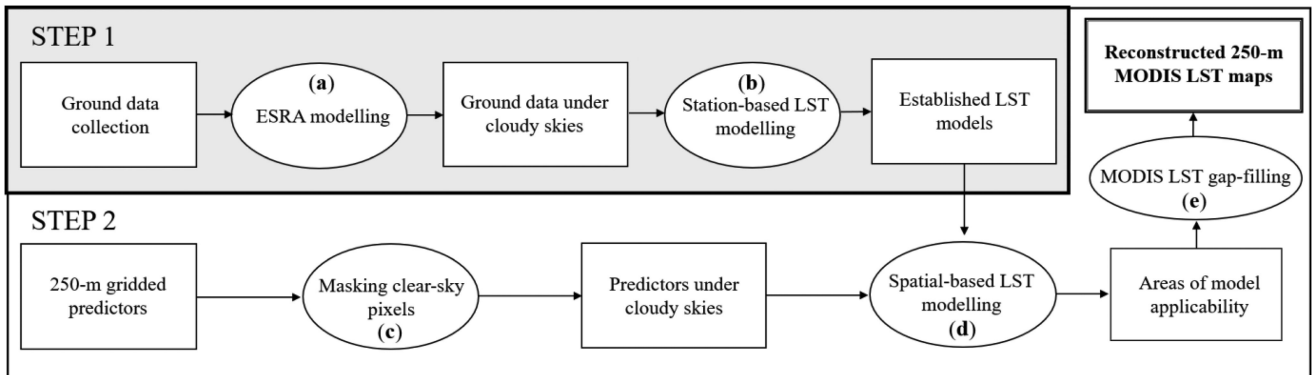

Fig. 2.   Workflow for LST gap-filling procedure under cloudy-sky conditions for MODIS data. While rectangular boxes refer to data used, ellipse shapes represent processing steps.

The 250-m air temperature maps for Trentino-South Tyrol region were obtained by interpolating the daily meteorological observations provided by the regional weather station networks of Meteotrentino for the Province of Trento and the Hydrological Department of the Province of Bozen/Bolzano. All observations were checked for quality and homogeneity and harmonized in a dense archive of more than 200 station series covering the region. The daily grids of TA_{mean} and TA_{max} were then derived for the period 1980–2018 by applying an interpolation method combining the reference mean climate, i.e., the climatology, and the daily temperature anomalies. Due to the mountainous terrain of the area, the interpolation applied a regression-based procedure

modelling the local relationships between temperature spatial gradients and orographic features, including elevation and slope characteristics, which were derived from the Digital Elevation Model (DEM) Copernicus EU-DEM v1.1[3] and then aggregated to the target 250 m resolution [65], [66]. Cross-validated average RMSE values in a spatial cross-validation approach for TA_{mean} and TA_{max} outputs were around 1.9 °C and 2.4 °C, respectively.

Daily solar radiation grids at 250 m resolution were derived by applying a geostatistical downscaling to the 2004–2018 daily

[3][Online]. Available: https://land.copernicus.eu/imagery-in-situ/eu-dem/eu-dem-v1.1

downwelling surface shortwave flux (DSSF) product derived from MSG/SEVIRI, available on the LSA-SAF system.[4] In particular, the sharpening of daily solar radiation (SW_{in}) was performed by means of a regression kriging (RK) in conjunction with the main topographic drivers, e.g., elevation, slope steepness and its orientation. In this scheme, the linear regression model was first estimated, the resulting residuals were interpolated onto the target grid through Ordinary Kriging with automatic fit of the variogram, and the final daily fields were obtained as sum of the spatialized residuals and regression predictions at each target grid cell. The average RMSE (bias) error was 2.64 MJ $m^{-2}day^{-1}$ (0.11 MJ $m^{-2}day^{-1}$) translating into the mean absolute percentage difference of 0.15 when compared to the ground-derived datasets.

In this article, we exploited remotely sensed surface albedo from a 16-day Terra/Aqua MODIS Albedo product (MCD43A3 Version 6) with 500-m pixel size [67]. The time-coincident MCD43A3 with good quality assurance (QA) flags were used for gap-filling of invalid MODIS LST. Additionally, an impact of landcover on LST was examined by parametrization of vegetation properties using aerodynamic roughness (z_0) and LAI (see Table III for details) [68], [69]. Spatially continuous LAI maps were obtained from 4-day Terra/Aqua MODIS LAI composites (MCD15A3H Version 6) at 500 m spatial resolution [70]. To increase spatial availability of LAI pixels, the 4-day MODIS LAI was upscaled to 14-day composite considering the highest quality of the QA flags as well as the closest acquisition time between station records and MODIS time overpass. While gridded albedo was only applied to the fitted models, LAI was used for both LST modeling and reconstruction of missing MODIS LSTs under cloudy-sky conditions. To keep spatial consistency with the reconstruction outputs, both MCD43A3 and MCD15A3H were disaggregated to 250-m pixel size using nearest neighbor resampling approach.

In order to identify cloud-covered areas for the LST reconstruction, we used invalid values that were assigned to the QA flags in the 1-km MODIS product. Since the focus of the article was on the LST reconstruction for vegetation analyses, daytime Terra MODIS LST (MOD11A1 Version 6) was utilized [71]. To examine the performance of the proposed method, we reconstructed missing pixels for six MOD11A1 images acquired in different seasons in 2014 (May 2nd, June 29th, July 8th, September 19th, October 11th, and 26th).

Areas of applicability for the reconstructed LST maps were determined by exploiting relationship between 250-m pixels within model vegetation groups (see Table I) and EVI from Terra MODIS Vegetation Indices (MOD13Q1 Version 6) granules [72]. In this article, we used the detailed land use landcover (LULC) data with minimum mapping area equal to 1600 m^2, as shown in Appendix [73]. The pixelwise selection procedure will be explained in Section II-CD. In addition, we applied daily 250-m MODIS snow cover mask to gridded predictors in order to exclude nonvegetated pixels from LST reconstructions [74].

C. Methodology

1) Model Concept: The Alpine region benefits from dense network of ground stations, which translates to time-series of climate data and generation of spatially continuous meteorological grids.[5] To take the full advantage of these 250-m inputs, we propose station-based modelling to reconstruct daytime Terra MODIS LST (MOD11A1) under cloudy-sky conditions at 250 m pixel size, that is a sufficient scale for capturing spatial details at regional level [75]–[78]. Subpixel mapping is considered as a reasonable solution in mountain regions characterized by complex structure of the landscape, where 1-km MODIS LST images cannot fully represent spatial heterogeneities of the terrain. The land surface temperature reconstruction was performed with two steps as follows:

1) Year-round LST modelling from station-based environmental variables under long-term cloudy skies; and
2) Applying the fitted models to cloud-contaminated MODIS LST pixels.

The conceptual scheme of the proposed method is summarized in Fig. 2.

The diurnal cycle of LST is highly affected by the surface energy balance and the surface thermal inertia that depend on ground characteristics, such as landcover, soil type, and its moisture [79]. Since clouds affect the energy budget of the ground, the LST modeling was defined under the assumption that LSTs beneath clouds are different than those under clear skies. In this context, we used the European Solar Radiation Atlas (ESRA) to define sky conditions for each hourly observation from station records [see Fig. 2(a)] [64], [80]–[82]. Determination of cloudy- and clear-sky observations was based on the hourly incident solar radiation (SW_{in}) from the meteorological stations and its corresponding maximum theoretical value computed from the ESRA model [60]. A ground-derived SW_{in} record was considered as a clear-sky observation provided that it exceeded 90% of maximum theoretical ESRA-based estimation, while the measured solar radiation with less than 50% of the maximum theoretical value was assigned to the cloudy-sky group. Additionally, the measurements registered two hours before and two hours after a respective observation had to meet the cloudy-sky criteria in order to extract long-term overcast observations.

Given a strong relationship between instantaneous air TA and ground-derived LST, daily mean air temperature (TA_{mean}) was considered as a baseline predictor in the LST modeling [7], [8], [60], [83], [84]. Fig. 3 presents the daytime and yearly cycle of the mean difference between hourly LST and daily TA_{mean} considering cloud-free and overcast conditions for all available observations (see Table I).

In general, the hourly [see Fig. 3(a)] and daily [see Fig. 3(b)] differences between LST and TA_{mean} under clear skies were noticeably bigger when compared to cloudy-sky variations. Overcast conditions alter the energy budget of land, resulting in smaller variations between LST and TA_{mean} [see Fig. 3(a) and (b)]. As shown in Fig. 3(a), cloud-free LST-TA_{mean} values varied with hours, with the biggest deviation reaching 9.2 °C close to

---

[4][Online]. Available: https://landsaf.ipma.pt

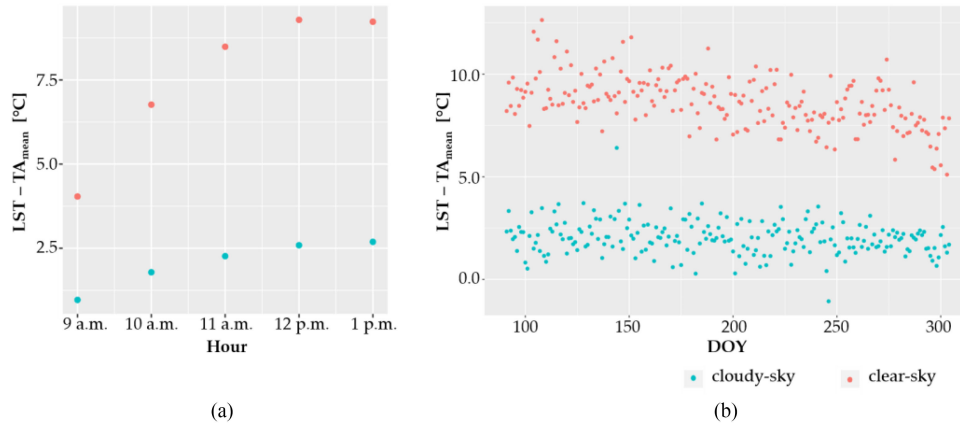[5][Online]. Available: https://doi.pangaea.de

Fig. 3.   Mean differences between hourly LST and daily TA_{mean} for all stations used in the study grouped by: (a) hour corresponding to approximate daytime Terra MODIS acquisition time and (b) day of year (DOY) between April and October.

TABLE IV
MEAN DIFFERENCE BETWEEN HOURLY LST AND DAILY TA_{MEAN} UNDER
CLEAR AND LONG-TERM CLOUDY SKIES FOR EACH STATION

Station	LST-TA_{mean} [°C]	
	Cloudy-sky	Clear-sky
Rotholz	2.60	7.66
Chamau	1.29	6.45
Früebüel	1.06	6.69
Neustift	2.76	8.51
Oensingen	3.70	10.16
Monte Bondone	4.07	12.86
Mazia 1	2.76	9.63
Mazia 2	3.84	13.31
Mazia 3	4.08	13.04
Mazia 4	3.74	15.23
Torgnon 1	4.17	13.18
Caldaro	1.43	4.13
Valle dell'Adige	1.53	7.83
Lavarone	0.07	2.82
Davos	-1.04	2.07
Renon	0.97	5.01
Torgnon 2	1.20	5.60

solar noon. For overcast conditions, however, the discrepancies between LST and TA_{mean} were smaller ($\leq$ 2.7 °C), and they were more consistent within a day. This resulted in hourly-based standard deviation equal to 0.71 °C that was approximately 1.5 °C smaller than under clear-sky conditions [see Fig. 3(a)]. Similarly, as for the hourly observations, the day-of-year (DOY) based differences under cloudy-sky conditions were fairly stable throughout the year when compared to clear-sky observations [see Fig. 3(b)].

An additional analysis performed for the individual stations showed that LST tends to be greater than TA_{mean} with increased values for clear-sky observations (see Table IV). While there was one station (Davos) with TA_{mean} greater than LST under cloudy skies, for the rest of the sites the mean differences were positive and ranged from 0.07 °C (Lavarone) to 4.17 °C in Torgnon 1. The mean variations between LST and TA_{mean} for cloud-free conditions were larger than for overcast conditions for all stations yielding values from 2.07 °C in Davos to nearly 15.2 °C in grass-covered Mazia 4 (see Table IV). The paired t-test verified that the clear-sky LST-TA_{mean} observations for the individual stations were significantly greater ($p < 0.001$) than the corresponding differences under cloudy-sky conditions.

Based on the abovementioned analyses (see Fig. 3, Table IV), daily mean air temperature was examined as a principal variable to explain LST deviations as described in further sections of the article.

2) Algorithms: LST observations under long-term cloudy-sky conditions were modeled by three different regression algorithms [see Fig. 2(b)]. A multivariate linear regression (MLM) model was used as a baseline estimator to explain the relationship between ground-based LST and independent variables. The MLM is considered as an intuitive tool with lower complexity for data interpretation, which makes it commonly used in modeling and preprocessing tasks [7], [9], [49]. As an alternative to the standard MLM, we exploited artificial neural network (ANN) and random forest (RF) [85]–[87]. Selection of these approaches was dictated by two main reasons. First, they belong to two algorithm families with different assumptions, which make them useful for comparison analysis [88]. Second, the ANN and RF have ability to account for both linear problems and nonlinearities between predictors and dependent variable. The algorithms have been successfully used in many studies, including spatial mapping and remote sensing enhancement tasks [9], [52], [89]. More detailed information about the algorithms is provided by Kuhn *et al.* [86].

3) Model Calibration and Evaluation: Spatio-temporal predictive tasks entail an appropriate data management and modelling strategies to retrieve reliable estimations for new locations. One of the most common problems regarding modelling from geographical features is the existence of dependence between predictors and time-neighboring observations resulting in model overfit that is revealed by well-fitted regression for training data and poor predictions beyond known points [9], [90].

Prior model training process, dependencies between predictors were investigated by exploiting variance inflation factor (VIF) to solve multicollinearity issue among features [91]. The VIF is defined as follows:

$$\text{VIF}_k = \frac{1}{(1 - R_k^2)} \tag{1}$$

TABLE V
RESULTS FROM THE HYPERPARAMETER OPTIMIZATION FOR THE MODELS WITH THEIR FINAL VALUES

Algorithm	Short description	Hyperparameter search grid		Final value
eNet	alpha: elastic mixing parameter lambda: regularization parameter	alpha: 0.0-1.0 lambda: 0.001-0.6	alpha$^{\mathrm{forest}}$: 1.0 alpha$^{\mathrm{agri}}$: 0.8, 1.0 alpha$^{\mathrm{grass}}$: 1.0	lambda$^{\mathrm{forest}}$: 0.05 lambda$^{\mathrm{agri}}$: 0.0, 0.05, 0.7 lambda$^{\mathrm{grass}}$: 0.0
ANN	size: units per hidden layer decay: weight penalty parameter	size: 1-10 decay: 0.0-0.5	size$^{\mathrm{forest}}$: 1, 9 size$^{\mathrm{agri}}$: 1, 2, 3 size$^{\mathrm{grass}}$: 1, 2, 3	decay$^{\mathrm{forest}}$: 0.0, 0.4 decay$^{\mathrm{agri}}$: 0.0 decay$^{\mathrm{grass}}$: 0.0, 0.1, 0.2, 0.5
RF	mtry: number of prediction variables randomly sampled as candidates at each split	mtry: 1-4	mtry$^{\mathrm{forest}}$: 2, 3 mtry$^{\mathrm{agri}}$: 2, 3, 4 mtry$^{\mathrm{grass}}$: 2	

ANN = feed forward network with one hidden layer, RF = random forest based on 1000 trees, eNet = elastic net model used as an alternative to the MLM. The abbreviation *agri* refers to permanent crops.

where the R_k^2 indicates the unadjusted coefficient of determination calculated by regressing the kth independent variable on the remaining predictors.

For regression tasks in spatio-temporal domain the overfitting problem is not only related to the redundant features but also to an incorrect model calibration or inappropriate predictor selection [9]. In this context, a model regularization needs to include these two aspects. Spatial cross validation (SCV) with a "leave-one-station-out" approach that excludes all observations of one station iteratively using station-fold splits (as k-fold subsets), and then compares all fold-driven simulations, could allow evaluating prediction power beyond training data, while simultaneously reducing autocorrelation between observations. On the other hand, forward feature selection (FFS) estimates the significance of predictors by inspecting possible model combinations and selects only those features, which improve model performance in terms of accuracy metrics [92]. In this article, we combined the FFS and SCV to determine the final features considering the highest model prediction performance in terms of its accuracy [9], [93], [94]. Average RMSE and R^2 together with their corresponding standard deviations (SD$_{\mathrm{RMSE}}$ and SD$_{\mathrm{R}}{}^2$) were calculated as evaluation metrics to choose the best modeling approach.

As mentioned previously, the regularization was performed by applying forward feature selection to all predictor variables in conjunction with the leave-one-station-out SCV [9]. The tuning was additionally conducted to obtain optimal algorithm hyperparameters for the models [95]. In the case of the ANN and RF, parameters for each model were evaluated within the iterative SCV process using tuning search grids (see Table V) [96], [97]. In addition, we applied elastic net (eNet) model to test regularization impact on the MLM. We performed multiple modeling for each vegetation group (see Table I) considering different combinations of hyperparameters in the search grids. The optimal values were chosen according to SCV accuracy scores.

Since the main aim of the calibrated models was to apply them to unseen gridded data, the test subsets were created during the spatial cross-validation approach to estimate model robustness beyond training points. The spatial predictive performance of all models (MLM, eNet, ANN, RF) was compared by conducting multiple paired t-tests.

In this article, for model creation we used Caret and CAST packages available in the R statistical software that contains the MLM, eNet, ANN, and RF model implementations from other R libraries [96]–[99].

4) Extension to Gridded Data: After the definition of the models, based on ground station data, they were applied to gridded predictors to reconstruct cloudy LSTs from MODIS LST at 250 m spatial resolution [see Fig. 2(c)–(e)]. Since year-round modeling was split into separate LULC-driven estimators, we defined potential areas for each model by considering similarities in predictor variable space.

In order to estimate model transferability, we made a quantitative comparison between data used for model training and gridded features representing new locations for the LST reconstruction. Similarity measure between a target pixel (i.e., a new point to predict) and training data was assessed by minimum Euclidean distance in the multidimensional predictor space with respect to an average distance between points used during training process [90]

$$d_{\mathrm{target}}^i = \min[d(i,j)] \tag{2}$$

where min [·] represents minimum function, *d(i, j)* indicates distance between a new point *i* and *j*th observation from training data, and $d^i{}_{\mathrm{target}}$ is a minimum distance between a new location *i*th and a point used in the modeling [96].

Based on this, a standardized distance (d$^\sigma{}_{\mathrm{target}}$) for each new location was derived, as shown in

$$d_{\mathrm{target}}^\sigma = \frac{d_{\mathrm{target}}^i}{d_{\mathrm{mean}}} \tag{3}$$

where d$_{\mathrm{mean}}$ indicates an average Euclidean distance from a target *i* to all training points.

Areas of applicability (AOA) for the considered models were defined based on the concept developed by Meyer and Pebesma [90]. We selected this approach because it deals with a problem

TABLE VI
SUMMARY OF THE MODEL EVALUATION MEASURES FROM MULTIVARIATE LINEAR REGRESSION, ELASTIC NET, NEURAL NETWORKS, AND RANDOM FOREST

Group	Algorithm	RMSE [°C]	SD$_{RMSE}$ [°C]	R^2	SD$_R{}^2$	Final predictors
	MLM	2.67	1.62	0.74	0.15	TA$_{mean}$, TA$_{max}$
Permanent crops	eNet	2.61	1.74	0.76	0.16	TA$_{max}$ - TA$_{mean}$
	ANN	2.74	1.51	0.72	0.13	SW$_{in}$
	RF	3.05	1.49	0.69	0.11	$\log(z_0)\alpha^{-1}$
	MLM	1.84	0.42	0.88	0.04	TA$_{mean}$, TA$_{max}$
Forest	eNet	1.84	0.45	0.88	0.04	SW$_{in}$
	ANN	1.84	0.42	0.88	0.04	TA$_{max}$ - TA$_{mean}$
	RF	1.91	0.41	0.86	0.04	
	MLM	2.07	0.32	0.77	0.07	TA$_{mean}$, TA$_{max}$
Grassland	eNet	2.08	0.32	0.77	0.07	TA$_{max}$ - TA$_{mean}$
	ANN	2.05	0.33	0.78	0.07	SW$_{in}$
	RF	2.12	0.32	0.77	0.07	$z_0 \cdot (h)^{-1}{}_{SD00}$

Underlined records represent final algorithms for reconstructing cloud-covered MODIS LST and their corresponding predictors (seventh column) selected in the forward feature selection approach (see Sections III-B and III-C for more details).

of model transfer into unknown environments that have never been seen by fitted regressions. This approach is relevant to reduce uncertainties in spatial predictions beyond the training data, especially in mountainous regions with fragmented landscape for which cross-validation provides only global accuracy metrics limited to feature variability covered by training observations [100], [101]. Therefore, AOA were determined considering the range of the predictor values used for establishing the models. Specifically, the AOA was derived from standardized distances based on training data records (d$^\sigma$$_{training}$) with respect to the spatial cross-validation folds as follows:

$$d_{\text{training}}^{\sigma} = \frac{d_{\text{training}}^{j}}{d_{\text{mean}}^{\text{training}}} \qquad (4)$$

where d_{training}^{j} represents minimum Euclidean distance between a *j*th training observation and a point from remaining station-fold subsets, and $d_{\text{mean}}^{\text{training}}$ indicates a mean distance between a *j*th location and other points included in other CV splits.

It means that $d_{\text{training}}^{\sigma}$ was derived based on training points that did not appear in the same station-fold subset in the CV (see Section II-C3) as we assumed that the model performance estimates (see Table VI) apply to $d_{\text{target}}^{\sigma}$, which is comparable to $d_{\text{training}}^{\sigma}$ values.

Model transfer to new geographic locations was realized by applying the 0.95 quantile of the $d_{\text{training}}^{\sigma}$ as a threshold for the target standardized distances ($d_{\text{target}}^{\sigma}$) [90]. Gridded data beyond that range were flagged as outliers (outside AOA), and thus, those areas were excluded from further LST reconstruction. Estimation of the AOA was performed in the CAST package implemented in the R software [98].

In addition to AOA, we determined potential locations for LST prediction by investigating spectral similarities between pure pixels represented by LULC-driven groups (see Section III-A) and mixed grid cells. Previous studies showed that land surface temperature is highly correlated with vegetation indices that capture spectral differences between plant species [31], [102], [103]. Thus, MODIS EVI (MOD13Q1 Version 6) was used for similar pixel extraction for vegetation groups defined in Table I. First, we extracted homogenous EVI with a minimum

threshold of 80% within 250-m mask obtained from the LISS-2013 landcover (Appendix, Fig. 9). We exploited time-series of EVI images acquired from 2014 to 2017 within months with phenological vegetation cycle. Target pixels were classified to the closest vegetation group using the following condition:

$$\left| \beta_i^T - \beta_{\text{target}}^T \right| < \sqrt{\frac{\sum_{n=1}^{n} \left(\beta_n^T - \beta_{\text{mean}}^T \right)^2}{n\,(n-1)}} \qquad (5)$$

where β_i^T indicates the closest homogenous pixel *i* to a target pixel β_{target}^T, T is a DOY corresponding to MODIS acquisition time, β_{mean}^T represents an average EVI value of available pure pixels β_n^T for a given DOY, n is number of homogenous pixels for each model group.

Pixels were assigned to a biome group if the majority of the individual β_{target}^T from the multiyear classification fulfilled the above constraint. Considering high landcover heterogeneity over the study area, some EVI pixels may contain fractional landcover, which hampers delineation of areas of applicability for the models. Many authors showed that LST of a nonpure pixel can be a linear mixture of subpixel components [104], [105]. In this context, when target pixels were classified to more than one group, fractional vegetation mask from the LULC map was generated, and weighted average values of surface temperature from respective biome-based models were computed (Appendix, Fig. 10).

III. RESULTS

A. LST$_{mean}$ − TA$_{mean}$ Comparison Under Cloudy Skies

Considering the complex character of the surface–atmosphere processes in the Alps, we first examined the overall relationships between ground-based LST$_{mean}$ and TA$_{mean}$ under-cloudy-sky conditions for each station independently. Fig. 4 illustrates the LST$_{mean}$ − TA$_{mean}$ scatterplots for sites located in forests and grasslands.

The regressions show a site-dependency driven by landcover of the stations (see Table I). The scatterplots represented by forest, however, approximated a 1:1 relationship more closely than sites covered by grasslands (see Fig. 4). For forest sites [see
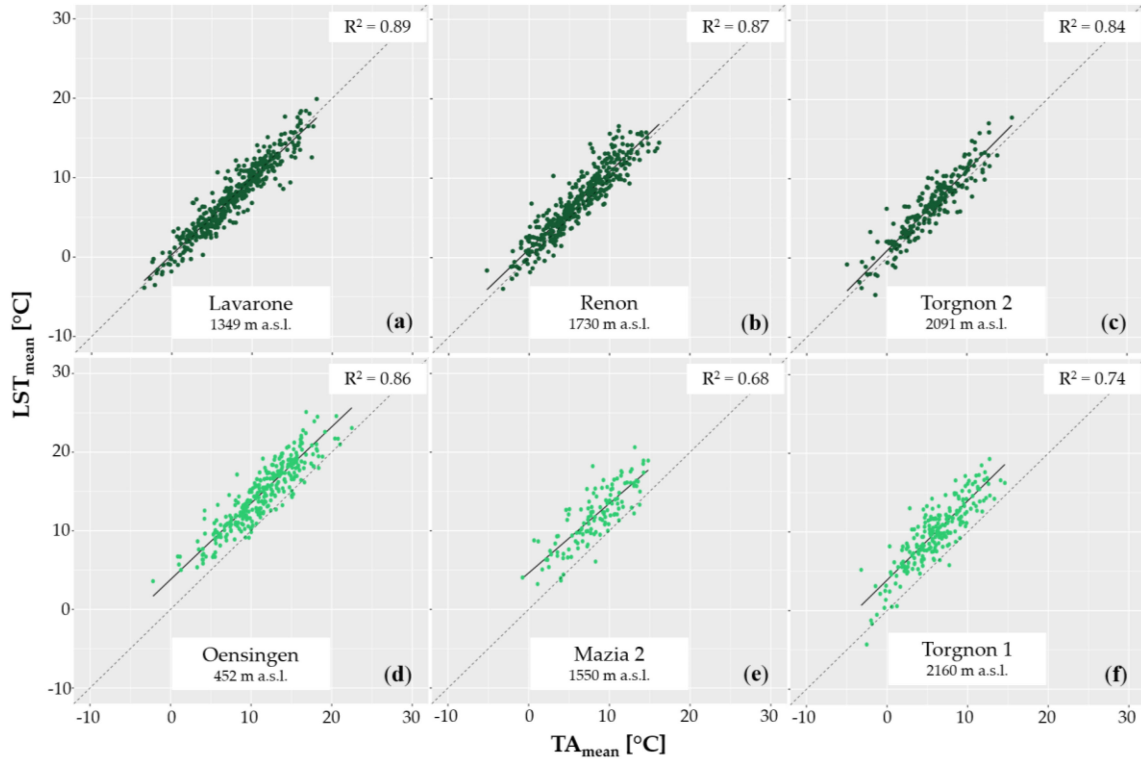
Fig. 4. Scatterplots between LST_{mean} and TA_{mean} under cloudy skies for six example weather stations covered by forest (in dark green) and grassland (in light green). LST_{mean} was calculated as an average from hourly LSTs recorded between 9 A.M. and 1 P.M. as an approximate range for daytime Terra MODIS acquisition time over the study area. Dashed lines in the scatterplots depict divergence between LST_{mean} and TA_{mean}.
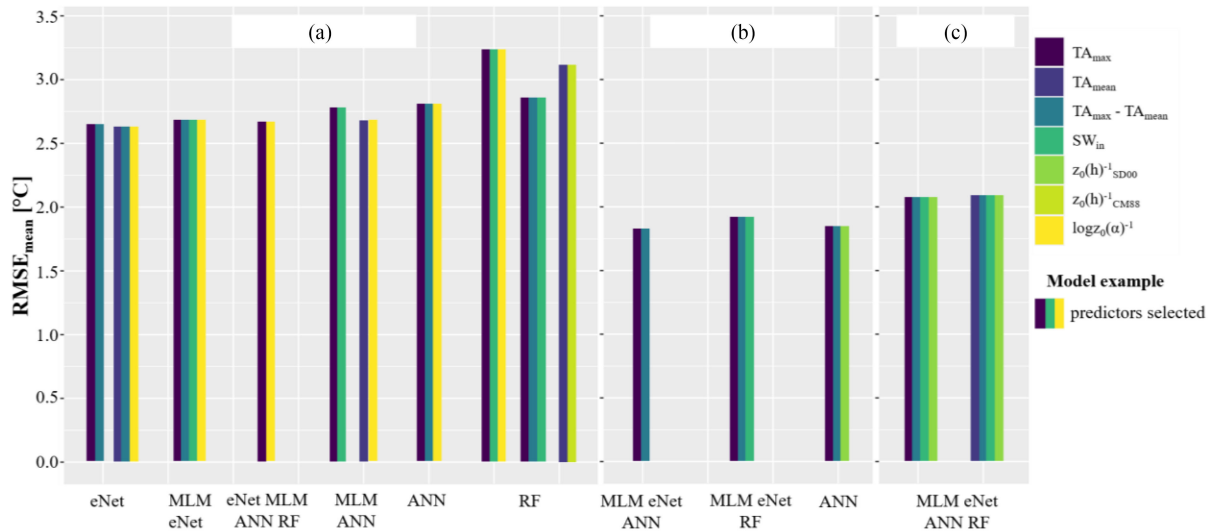

Fig. 5. Selected combinations of predictors evaluated by the averaged RMSE ($RMSE_{mean}$) from all algorithms for: (a) permanent crops, (b) forest, and (c) grassland during the FFS procedure. $RMSE_{mean}$ was computed considering hour-round LST models corresponding to MODIS acquisition time.

Fig. 4(a)–(c)] LST_{mean} and TA_{mean} under cloudy skies ranged roughly the same values regardless their elevation, while TA_{mean} for grass-covered areas may underestimate surface temperatures [see Fig. 4(d)–(f)]. In particular, LST_{mean} over grasslands tends to be higher than TA_{mean} and the difference grows with temperature, especially at higher altitudes [see Fig. 4(e)–(f)]. Considering different $LST_{mean} - TA_{mean}$ behavior among the landcover types, the LST models were built based on aggregated stations that represent similar environmental conditions

(see Table I). Forest, grasslands, and permanent crops were considered as three separate model groups for the final LST reconstruction.

B. Selected Predictors

Although LST can be explained from TA_{mean}, the biophysical impact of landcover on LST, as shown in Fig. 4, suggested incorporation of additional variables that can describe complex
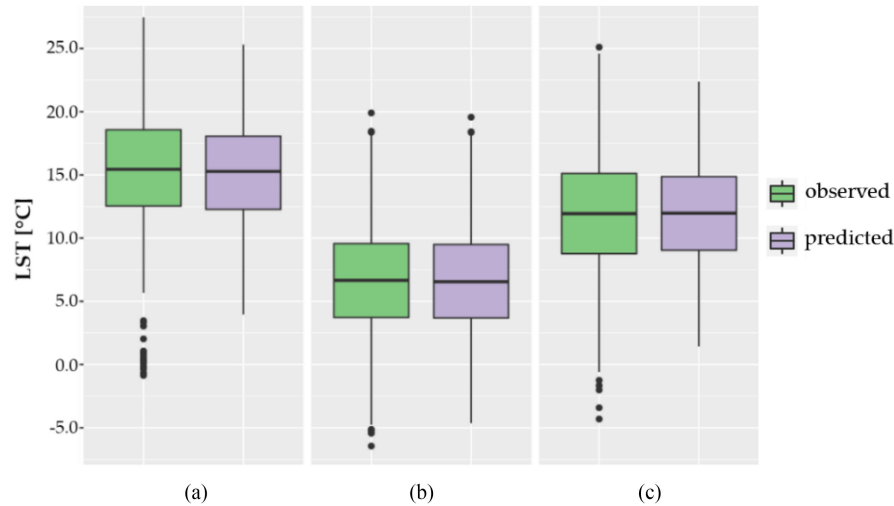
Fig. 6. Comparison between observed and predicted LSTs from the final models for: (a) permanent crops, (b) forest, and (c) grassland, considering combined MODIS-like time splits.

interplay between ground and atmosphere. The final features for each model group, as explained in Section II-C3, were selected using FFS procedure in the SCV approach. Fig. 5 displays selected explanatory variables for each model group based on all algorithms applied. Their relevance was evaluated by RMSE, averaged with respect to MODIS-like time splits ($\text{RMSE}_{\text{mean}}$).

As can be observed in Fig. 5, LSTs over grassland and forest ecosystems, regardless of the algorithm used, were explained by one and three unique sets of predictors, respectively. During the FFS procedure for forest group, parameters were mainly reduced to air temperature (TA_{max}, TA_{mean}) and daily incoming solar radiation yielding $\text{RMSE}_{\text{mean}}$ ranging from 1.82 °C to 1.92 °C, while for grass-covered areas vegetation structure parameter ($z_0 \cdot h^{-1}{}_{\text{SD00}}$) was additionally selected as significant predictor in all MODIS-like time models [see Fig. 5(b) and (c)]. Due to complex structure of the permanent crops, which influences temporal variability in LST, eight different combinations of features were chosen, and they varied between algorithms [see Fig. 5(a)]. Considering all predictor sets of permanent crops, albedo-based product $-\log(z_0) \cdot (\alpha)^{-1}$ and air temperature reported the highest frequencies yielding 69% and 100% of times they occurred in the models, respectively.

C. Model Comparison and Assessment

Along with the predictor selection procedure, performance of the proposed LST reconstruction method was compared for each vegetation group separately (see Table I). As mentioned previously in Section II-C3, we checked regression overfit on test data in the SCV approach to evaluate predictive strength of the fitted models. Table VI shows averaged accuracy scores obtained from each algorithm with combined MODIS-like time splits.

As can be observed in Table VI, the proposed LST reconstruction concept gave quite similar accuracy statistics for each vegetation classes with small differences between the tested algorithms. Considerably uniform RMSE (R^2) metrics, regardless

of the algorithm used, were present for forest and grassland ranging from 1.84 °C to 1.91 °C (0.86 to 0.88) and 2.05 °C to 2.12 °C (0.77 to 0.78), respectively (see Table VI). The greatest errors appeared over permanent crops yielding overall cross-validated RMSEs from 2.61 °C (MLM) to 3.05 °C using RF algorithm. Similar situation applied to standard deviation of RMSE (SD_{RMSE}) and R^2 scores ($\text{SD}_{\text{R}}{}^2$), resulting in higher values for all tested algorithms when compared to forest and grass-covered model groups (see Table VI).

The multivariate linear regression was found as the best LST estimator with SCV RMSEs (SD_{RMSE}) of 2.67 °C (1.62 °C) and 1.84 °C (0.42 °C) for permanent crops and forest, respectively. Although slightly lower RMSE over permanent crops was identified for the eNet, we selected MLM due to its smaller SD_{RMSE} score (see Table VI). For forest group eNet and ANN gave the same results (RMSE = 1.84 °C) when compared to the linear model, however, we excluded these algorithms because of their longer computation time to tune hyperparameters (see Tables V and VI). On average, for the grassland models, we obtained the highest predictive performance from ANN yielding 0.78 and 2.05 °C for R^2 and RMSE, respectively. Slightly lower accuracy statistics were noted for MLM and eNet with a 1.5% increase in RMSE. Random forest depicted the poorest predictive performance among all LULC model groups (see Table VI).

The performance of the regressions differed at the level of landcover classes. For forest we found smaller errors, while larger deviations in LSTs appeared over grasslands and permanent crops with 12% and 48% increases in RMSE when compared to forest accuracy metrics (see Table VI). Due to the unique atmospheric coupling of forest, this class maintained the strongest LST-TA relationship ($R^2 \approx 90\%$) among all model groups (see Fig. 5, Table VI) [61], [106]. LSTs over grassland and permanent crops with a relatively smaller impact of turbulent mixing were additionally explained by other biophysical parameters, e.g., surface albedo, leaf area index, and aerodynamic roughness. Instability of crops model group revealed by higher SD_{RMSE} and $\text{SD}_{\text{R}}{}^2$ values documented in Table VI, can be

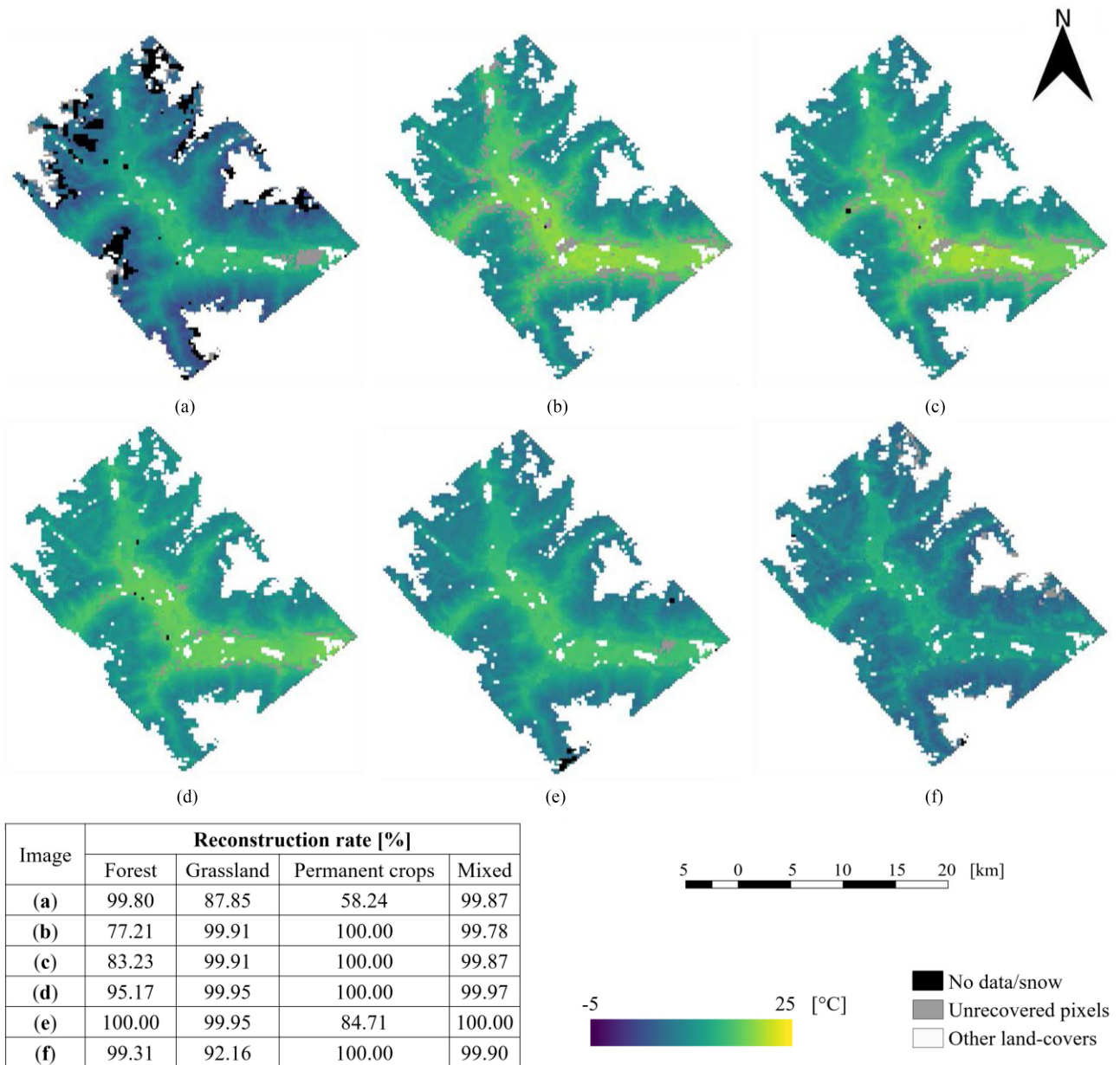| Image	Reconstruction rate [%]			
	Forest	Grassland	Permanent crops	Mixed
(a)	99.80	87.85	58.24	99.87
(b)	77.21	99.91	100.00	99.78
(c)	83.23	99.91	100.00	99.87
(d)	95.17	99.95	100.00	99.97
(e)	100.00	99.95	84.71	100.00
(f)	99.31	92.16	100.00	99.90

Fig. 7. Results of the proposed subpixel LST reconstruction of 1-km daytime Terra MODIS LST for long-term cloudy skies acquired on (a) May 2, 2014, (b) June 29, 2014, (c) July 8, 2014, (d) September 19, 2014, (e) October 11, 2014, and (f) October 26, 2014 in Vinschgau/Venosta. The attached table presents rate success of reconstructions for each vegetation group (see Appendix). According to the QA layer all original MODIS LST matrices were 100% covered by clouds.

related to the limited number of samples and heterogeneities of the combined land-use types (orchards and vineyards) incorporated in the modeling.

Considering the averaged accuracy statistics in Table VI, we achieved the strongest performance from ANN for grassland, while linear model gave the best results for permanent crops and forest groups. Therefore, only these algorithms were considered in the further analyses to reconstruct MODIS LST pixels obscured by clouds.

To compare prediction performance of the vegetation groups we investigated distribution of ground-based LST with their corresponding values predicted by the selected algorithms (see Fig. 6). On average, the interquartile ranges (IQR) of observed LSTs for all vegetation groups were in accordance with predicted

data. We found that the models were incapable to reconstruct observations beyond the IQRs, especially over grasslands and permanent crops [see Fig. 6(a)–(c)]. These patterns were mainly present for very low and high values (shown as circles), which appeared rarely in the models. Generally, this demonstrates that the chosen algorithms were able to capture LST variability with respect to different landcovers.

D. LST Reconstruction Under Cloudy-Sky Conditions

In the second part of the LST reconstruction the regressions were applied to gridded variables to estimate missing 250-m MODIS LST under cloudy-sky conditions. The outcomes of restoring invalid MODIS LSTs are presented in Fig. 7.
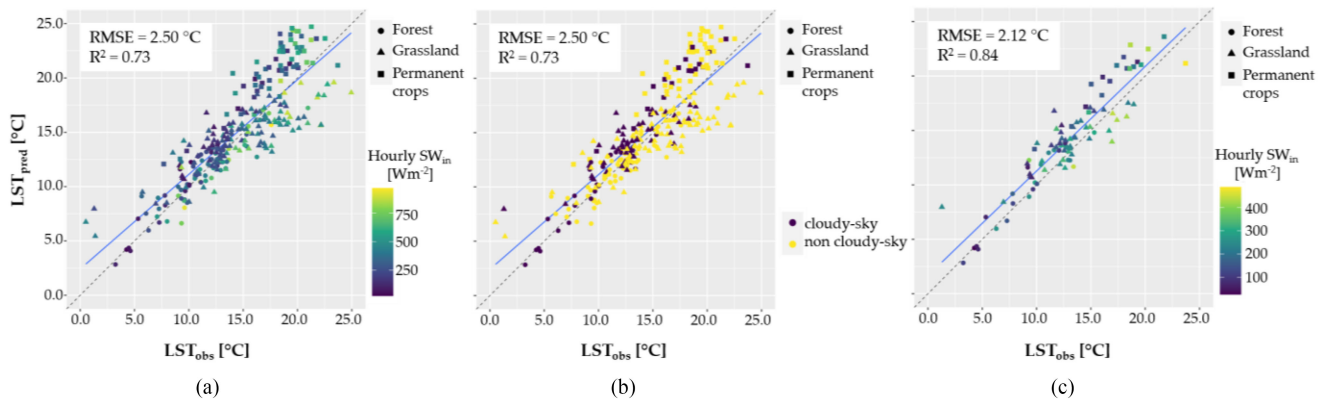
Fig. 8. Scatterplots between LST from ground measurements (LST_{obs}) and recovered values (LST_{pred}) based on the MODIS acquisition dates for the year 2014 with respect to: (a) instantaneous solar radiation (hourly SW_{in}), (b) sky conditions, (c) available stations with reduced number of observations. Noncloudy-sky conditions in Fig. 8(b) refer to station records that were neither classified as long-term cloudy-sky nor clear-sky observations. The validated sites are located in relatively uniform areas with minimum 85% of homogeneity for related land-cover types within 250 m pixel [73], [107].

As demonstrated in Fig. 7, the approach proposed in this article provided a satisfactory data recovery over the study area. Invalid values were effectively predicted and LST downscaling to 250 m spatial resolution allowed simulating LST variability at subpixel level. For all images, regardless their acquisition date and observing time, more than 92% of blank pixels were filled properly. The highest reconstruction rate was observed for scenes recorded in late summer and autumn [see Fig. 7(d) and (e)] and ranged from 97.59% to 99.66% on October 26th and 11th, respectively. For other three dates [see Fig. 7(a)–(c)], however, we noticed larger number of unrecovered pixels ($\leq$ 7.16%) that were classified as outliers by the models. On June 29th and July 8th areas of nonapplicability were identified for forests located in the center of the main valley and on its edges [see Fig. 7(b)–(c)]. Slightly less unpredicted pixels (3.75%) were found on May 2nd, which corresponded to high-mountain grasslands and permanent crops in the main valley [see Fig. 7(a)]. We found that the increased proportion of invalid LSTs, as seen in Fig. 7, may have occurred because of the smaller number of samples with cloudy-sky conditions and limited variability of observations to fit the models. This can be explained by different meteorological conditions in summer, with less intense and shorter cloud cover periods when compared to spring and autumn seasons. In addition, some pixels were not predicted due to coarse resolution of gridded parameters, such as MODIS LAI or albedo products. These factors had a negative impact on the LST reconstruction over the entire study area.

The reconstructed maps generally follow thermal patterns of the study area with higher temperatures in the valleys and colder conditions at high altitudes. On average, pixels of permanent crops located in the southwestern part of the region had relatively higher temperatures when compared to other biome groups situated at higher altitudes. We found that lower LST values were obtained over grasslands and forests. In contrast to the permanent crops, these biomes exhibited higher spatial heterogeneities with regard to terrain and thermal variability. This was confirmed in grass-covered areas with high deviations in elevation and LST equal to 546 m and 3.65 °C, respectively. Although for forest and grassland we noted similar thermal variability, standard

deviation of elevation for the latter vegetation group was over 200 m greater than for forest.

In addition, the reconstructed LST maps were compared with clear-sky MODIS LST grids acquired on temporally adjacent days (May 4th, July 1st, September 22nd, October 27th). Table VII shows an overview of statistical measures obtained from LSTs under cloudy skies (see Fig. 7) and their corresponding original MODIS images.

As shown in Table VII, the averaged differences in LST between clear-sky MODIS and the reconstructed grids revealed a cooling role of thick cloud cover that reduces amount of incoming shortwave radiation. In general, mean surface temperatures for clear-sky MODIS maps were higher than for the reconstructed grid cells, although the differences varied between time acquisitions. The largest deviations could be observed during spring and summer, with a maximum difference of 4.54 °C between June 29th and July 1st (see Table VII). Although higher values of the clear-sky MODIS LSTs generally indicate a stronger impact of solar radiation on the surface heating process, LST_{mean} on October 26th was very close to the average from MODIS LST acquired one day later (see Table VII).

Due to the complex land surface interactions in highly heterogenous mountain ecosystems, the restored LST pixels could have been additionally explained by other predictors that influence surface thermal properties, such as landcover classes, biomass content, or surface albedo (see Fig. 5, Table VI). On the other hand, 1-km MODIS data may not represent LST variability at the subpixel scale of the reconstructed maps resulting in lower LST values over the study area.

E. Validation With In Situ *Data*

To assess the effectiveness of our LST reconstruction, we performed a quantitative assessment by comparing station-based LSTs with their corresponding gap-filled pixels at 250 m spatial resolution for the entire year of 2014. Validation results are illustrated in Fig. 8.

The evaluation results indicate a close agreement between ground measurements (LST_{obs}) and the LST reconstructions

TABLE VII
ANALYTICAL COMPARISON BETWEEN THE RECOVERED LST AND THE TIME-COINCIDENT ORIGINAL MODIS DATA, AVERAGED FOR THE STUDY AREA

Reconstructed cloudy LST		Clear-sky MODIS LST	
date	LST_{mean} [°C]	date	LST_{mean} [°C]
2 May 2014	8.50	4 May 2014	10.41
29 June 2014	12.95	1 July 2014	17.49
19 September 2014	12.56	22 September 2014	13.60
26 October 2014	8.69	27 October 2014	8.72

Clear-sky MODIS LST maps for the remaining recovered days (July 8, 2014, October 11, 2014) were not available.

TABLE VIII
LOCAL COMPARISON OF RMSE AND BIAS VALUES BETWEEN *IN SITU* DATA AND RECONSTRUCTED GRIDS FOR CLOUD-COVERED MODIS LST PIXELS (DERIVED
FROM QA FLAGS) FOR THE FOUR STATIONS BASED ON TIMESERIES FROM 2014

Station	Reconstructed LST RMSE [°C] (BIAS [°C])	
	all cloudy-sky conditions (long- & short-term)	long-term cloudy-sky conditions
Caldaro	3.26 (-2.85)	2.81 (-2.38)
Lavarone	1.37 (0.12)	1.24 (-0.44)
Mazia 1	2.40 (-0.29)	2.42 (-1.47)
Mazia 2	2.88 (1.10)	1.57 (-0.71)

The reconstruction results are shown for all cloudy-sky conditions and for observations under long-term cloudy-sky conditions [see Fig. 4 and Fig. 8(c)].

(LST_{pred}). Considering all available *in situ* observations for the time acquisitions in 2014, the proposed approach was able to predict missing values with average R^2 of 0.73 and RMSE equal to 2.50 °C and [see Fig. 8(a) and (b)]. As can be observed in the scatterplots [see Fig. 8(a)–(c)], the estimated grids have a relatively strong coherence with the stations, however, some observations depicted divergence from a 1:1 relationship. The largest deviations occurred for the agricultural (Caldaro) and grass-covered sites (Mazia 1, Mazia 2) with higher values of the RMSE and instantaneous SW_{in} (over 500 Wm^{-2}), which reflects no presence of long-term cloudy skies during MODIS acquisition times [see Fig. 8(b)]. From this aspect, we eliminated those points from further analysis and achieved better evaluation results yielding 2.12 °C and 0.84 for RMSE and R^2, respectively [see Fig. 8(c)]. Considering each station separately, accuracies of the LST reconstruction under long-term cloudy-sky conditions differed between stations with the lowest errors for Lavarone and Mazia 2 (RMSE = 1.24–1.57 °C) and higher ones for Mazia 1 and Caldaro (RMSE = 2.42–2.81 °C) (see Table VIII). Similarly, biases between observed and predicted LSTs were dependent on the site location. In general, for Caldaro and Mazia 1, regardless of sky conditions, the model led to overestimation ranging from −2.85 °C to −2.38 °C and −0.29 °C to −1.47 °C, respectively (see Table VIII). While LST under all cloudy-sky conditions (long-term and short-term cloudy sky) was underestimated at some sites (specifically at Lavarone and Mazia 2), on average LST predictions under long-term cloudy skies were higher than the observed values. Overall, the reconstructions perform better for long-term cloudy-sky observations with lower RMSE values when compared to all cloudy-sky conditions (see Table VIII).

Such discrepancies, as shown in Fig. 8 and Table VIII, may have appeared because of differences in cloud cover conditions defined by the models and MODIS QA layer. A possible explanation is that although MODIS cells were classified as overcast during satellite observing time, those LSTs might not have been influenced by the long-term cloudy-sky conditions of our approach. This led to lower values of the reconstructed temperatures when compared to the ground measurements (see Table VIII, Fig. 8). In addition, spatial heterogeneities of land surface over the Alps could not have been captured by coarse resolution of gridded predictors, such as solar radiation, LAI, and albedo products (see Table III). These factors would have impacts on the accuracy of the gap-filling models leading to biases in the computation of the actual LSTs (see Table VIII).

To test the potential impact of the meteorological input uncertaintities on the model outputs under cloudy skies, we additionally predicted LSTs using the gridded datasets that were perturbated with input uncertainties of Type B by including their ±100% values to the input grids for the year 2014 [108]. The reconstructed pixels were assessed in terms of RMSE and percentage LST change with respect to *in situ* observations and original LST predictions, respectively. In general, among all predictors analyzed, we observed the biggest model deviations influenced by TA_{max} ranging from ±16% for Lavarone (forest) to ±8% for grassland (Mazia 1, Mazia 2) and permanent crops in Caldaro (see Appendix, Fig. 11). For other variables we observed smaller impact on the LST estimations. As shown in Fig. 12, RMSEs obtained between ground-derived and modelled LSTs (using both source and modified parameters) depended

on model biome with the largest absolute differences ($\sim$1 °C) for permanent crops (Caldaro) when TA_{mean} and TA_{max} were perturbated.

IV. DISCUSSION

A. Advantages of the Proposed Reconstruction

Thermal remote sensing images are prone to overcast conditions resulting in spatial gaps in LST data. Although many LST reconstruction methods were developed, their implementation is hampered either due to rarely available biophysical parameters or coarse resolution outputs, which makes them irrelevant in heterogenous environments. To overcome these limitations, the main objective of this article was to develop a robust procedure for restoring invalid coarse-resolution MODIS LSTs at 250 m spatial resolution by combining data-driven modeling from meteorological stations with physical-based approach to retrieve variables under long-term cloudy-sky conditions. The restored LST maps for six selected MOD11A1 images demonstrated the effectiveness of the AI-based reconstructions among all vegetation groups. The fitted models were able to identify parameters playing a key role in explaining LST variability driven by different landcovers. SCV with high coefficients of determination and relatively small errors confirmed the strong model performance, yielding on average an R^2 of 0.80 and a RMSE of 2.19 °C. From a visual assessment of the restored maps, regardless of different seasons, no notable irregularities in LST patterns were observed.

Due to lack of *in situ* measurements in 2014 for all sites, the gap-filled LST images were validated with observations from four available stations (see Fig. 8, Table VIII). Results demonstrated that predicted LST data were in accordance with ground-based records obtaining R^2 of 0.84 and RMSE of 2.12 °C. Compared with other reconstructions dealing with mountainous areas, our approach showed satisfactory evaluation scores. On average, Ke *et al.* [48] and Sun *et al.* [109] obtained lower accuracy with RMSEs ranging from 1.42 K to 3.16 K. Similarly, the SEB-based methods implemented by Yu *et al.* [29] and Yang *et al.* [32] led to weaker correlation between observed and predicted LSTs resulting in increased RMSEs ranging from 3.16 °C to 4.78 °C. However, we should keep in mind that these outcomes depend on site locations and are affected by accuracy of input data and spatial heterogeneity of study area.

This article demonstrated that surface temperatures under cloudy-sky conditions differ significantly from those under clear skies leading to greater differences between LST and daily TA_{mean} (see Fig. 3, Table IV) [60], [110]. Although they are correct from geostatistical point of view, they should not be used for retrieval of actual thermal conditions of the surface. On average, quantitative comparison between reconstructed maps and temporally adjacent clear-sky MODIS pixels showed that LSTs under cloudy-sky conditions were smaller when compared to valid datasets (see Table VII). This indicates an impact of clouds on amount of incident shortwave radiation, which regulates the land heating process. In this case findings from this article are not in agreement with spatio-temporal gap-filling proposed by Weiss *et al.* [44], Sun *et al.* [109], Li *et al.* [111], and Sarafanov *et al.*

[43] who predicted overcast surface temperatures from adjacent cloud-free pixels.

The developed AI-based approach provides more accurate understanding of additional controls on land surface temperature at local scale. Although strong correlations between LST and TA_{mean} under overcast conditions were observed (see Fig. 4), applying auxiliary variables to the models helped to explain LST variations among different vegetation groups. Based on preliminary tests, a split into separate landcover classes, which was also found favorable by Huang *et al.* [7], improved the accuracy of the models resulting in unique selection of final algorithms and predictors for each analyzed biome (see Fig. 5, Table VI). Permanent crops and forest models achieved the most satisfactory results from multivariate linear regression, while for grasslands the highest prediction performance was obtained using neural network algorithm. Forward feature selection revealed impacts of different factors controlling LSTs in heterogenous ecosystems. Similar to the results of Bertoldi *et al.* [53] and Mildrexler *et al.* [61], forest maintained the strongest relationship with daily air temperature (TA_{mean}/TA_{max}), while agricultural and grass-covered areas were additionally influenced by incident shortwave radiation and surface properties, such as albedo, aerodynamic roughness, and biomass content (see Figs. 4 and 5). The method developed in this article works well for the areas with clouds, which makes it comparable to physical-based LST reconstructions [30], [112]. Additionally, it does not require rarely available input parameters to describe complex physical mechanisms between ground and atmosphere.

Although our reconstruction approach showed a strong performance, about 7% of pixels of the study area were not predicted due to intentionally imposed constraints on the models (see Fig. 7). Prediction power of the reconstruction is limited by SCV strategy and similarity factors (Euclidean distance and spectral similarities in predictor variable space) that compare coherence between station-based training dataset and gridded predictors. These factors reduce areas for LST estimation to known environments where reconstruction errors apply. In this context, this approach seems to be objective in terms of spatial predictive tasks into new areas by avoiding locations with nonstandard observations identified by models [9], [90], [109].

B. Limitations

The proposed gap-filling approach exhibits large potential for producing high quality LST maps. Nevertheless, reliable reconstructions of LST in the Alps still pose challenges, mainly due to landscape heterogeneities and thermal variability in complex mountain environments.

Despite strong correlation between gridded data and ground measurements, the RMSE is 2.12 °C, which reflects that for some points prediction performance was still poor. Such discrepancies are likely related to input parameters leading to overestimation or underestimation of the restored maps. Differences in spatial scales between station records and gridded predictors, e.g., surface albedo, solar radiation, and air temperature can explain errors in the reconstructed data. Furthermore, the black antihail net used to protect the orchards (Caldaro) may introduce some

bias in the final LST output. In addition, some remotely sensed variables, including leaf area index and surface albedo were obtained from composite products (4-day MCD15A3H and daily 16-day MCD43A3 products), which introduces uncertainties associated with neglected temporal variations. In this context, more advanced daily interpolation methods could be explored [113]–[115].

When comparing the cross-validation results (see Table VI) with other data-driven methods [50]–[51], we found that our evaluation measures had less satisfactory scores. Wu *et al.* [50] obtained considerably stronger model performance with the CNN algorithm, attaining RMSE below 1 °C. Similarly, good results were reported by Zhao and Duan [51]. The authors applied random forest model from clear-sky pixels to cloud-covered MODIS LST with RMSE of 1.14 °C and R^2 equal to 0.94. Such discrepancies between our method and the abovementioned [50], [51] could be explained by a relatively small number of observations for the agricultural landcover class, which led to instability of the model reflected by greater deviations in RMSE between cross-validated ensembles. In fact, diversified character of the permanent crops (orchards and vineyards) and the resulting data randomness had an additional impact on the model performance. Therefore, further study will concentrate on the extension of ground data by augmenting the timeseries of underrepresented training data for modelling prior to LST reconstructions [116], [117]. Since recurrent neural network can learn patterns and associations between sequential data over time, deep learning models, such as the long short-term memory (LSTM) algorithm exhibit a great potential in generating high-quality observable variables for better model training effects [118]. In addition, combining ancillary ground observations outside the study area along with postprocessed outputs from physical models would be beneficiary to learn new spatio-temporal input parametrizations of predictors [119]. On the other hand, the performance of the discussed methods [50], [51] relied on low-resolution satellite-based inputs and random cross-validation strategy, which makes them less strict and more prone to autocorrelation than our "leave-one-station-out" SCV method [9]. Additionally, our approach exploits data that capture spatial detail at station level, which translates to stronger thermal variability when compared to heterogeneous information from coarse resolution MODIS and MSG/SEVIRI LST pixels. Therefore, the prediction errors for our method can be generally acceptable.

While the predictions were robust in areas with high-frequency cloudy-sky conditions, in some cases cloud-covered pixels from MODIS QA layer could lead to disagreement between reconstructions and their actual temperatures. When comparing our estimations to ground data, we found that increased proportion of solar radiation caused underestimation of restored values (see Fig. 8, Table VIII). While LST reconstruction was resilient in areas with high-frequency cloudy-sky conditions, the method was limited for short-term cloudy skies. The proposed method assumes that overcast conditions are present when minimum 5-h constant cloudiness is recorded. Thus, the approach is suitable for long-term overcast conditions with thick clouds. Otherwise, it can lead to underestimation of LST values, which is related to less intense insolation blocked by clouds. Thus, developing an extended approach for diversified overcast conditions could bring to significant accuracy improvements to the LST reconstruction over complex Alpine ecosystems.

Finally, the developed relationships are tuned to the ecosystems that characterize the study area. However, they could be easily extended to different regions if new observations (e.g., representing unique climatic conditions and surface properties) were provided. From this point of view, the method is less general than other data-driven approaches utilizing spatial information from remote sensing measurements [50], [51], [120], [121], because it specifically aims to gap-fill LST over Alpine regions, which are often under-represented in wide-ranging models. Nonetheless, LST reconstruction over different areas is still feasible, provided that required variables are available.

V. Conclusion

Cloud cover has a significant impact on quality of remotely sensed LST observations, especially in high-frequency overcast areas, such as complex mountain regions. Therefore, a robust reconstruction of actual LST is a major research priority.

To address this problem, we presented a new method to reconstruct MODIS LST values under cloudy skies from station-based models at subpixel (250 m) spatial resolution. The proposed approach reconstructs actual thermal conditions of land surface under cloudy skies as an alternative way to the SEB-based methods that require complex parameters and are computationally expensive. Results demonstrate that the proposed data-driven analysis is capable of restoring invalid MODIS maps in a very robust way.

The reconstructed maps have reasonable LST values when compared to temporally neighboring clear-sky MODIS days. The validation against *in situ* data confirmed the strong agreement between estimations and ground observations. The performance of the models had satisfactory results. Prediction power showed landcover dependency resulting in individual predictors for each biome. Overall differences in RMSEs between machine learning algorithms and linear regression were minor for forest and permanent crops, while for grassland neural networks slightly improved the performance. At level of single vegetation groups, RMSE values ranged from 1.84 °C in forest to 2.67 °C for permanent crops.

Notably, it should be mentioned that the restored maps represent LSTs under long-term cloudy skies and may underestimate LST cells affected by brief overcast conditions. Therefore, future research should include an implementation of a hybrid approach for recovering missing pixels affected by short-term and long-term cloud contamination. Moreover, additional work will focus on the development of the enhanced reconstructions under long-term cloudy-sky conditions to increase spatial prediction performance of the established models. In parallel to the gap-filling procedure, data enhancement will be also applied to clear-sky observations of 1-km MODIS LST data to produce the full collection of 250-m resolution images considering different sky conditions. Furthermore, the proposed reconstruction

method by applying the AI-models can be extended to other low-resolution TIR sensors, such as Sentinel-3 SLSTR to provide data continuity for the study area. The availability of a spatially and temporally continuous set of thermal data would allow monitoring multitemporal trends of thermal conditions of the surface. These outputs could be value-added products for studies related to climatology, drought detection, and sustainable agriculture production, where land surface temperature is a baseline information for monitoring ecosystem dynamics over high frequency cloud-covered areas, such as mountain regions.
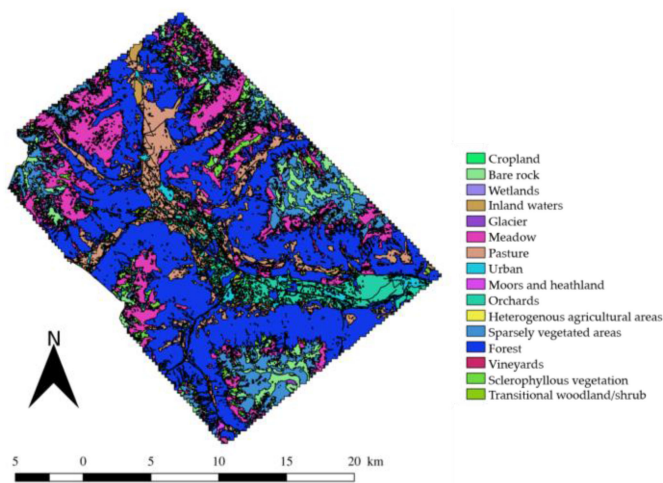
APPENDIX

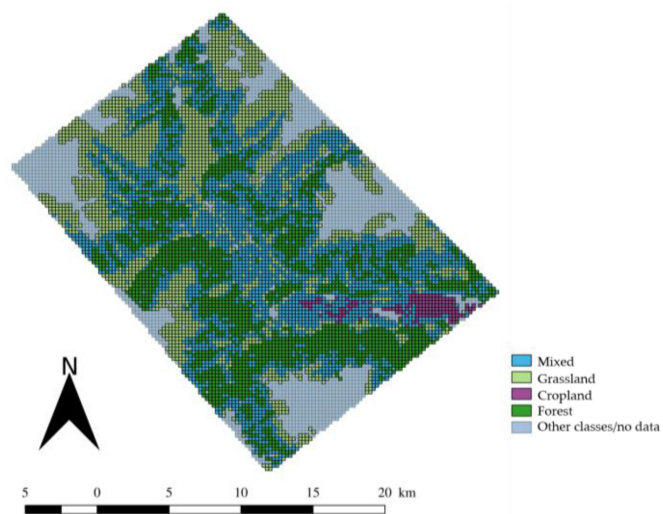Fig. 9. Detailed land use landcover (LULC) map from the LISS-2013 cropped to the reconstruction area.

Fig. 10. 250-m fractional vegetation map from the LISS-2013 for the landcover-based reconstruction models. Group "mixed" indicates 250-m pixels with more than one vegetation biome.
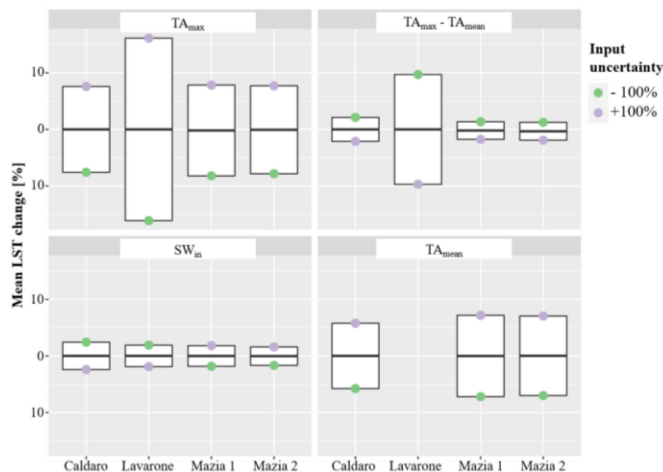

Fig. 11. Mean change in modeled LSTs with respect to surface temperature estimations from source meteorological input and the selected models (see Table VI) for the year 2014. Each climate predictor (TA_{max}, TA_{mean}, $TA_{max}-TA_{mean}$, SW_{in}) was perturbed by its uncertainty and included in the model together with remaining (unchanged) variables.
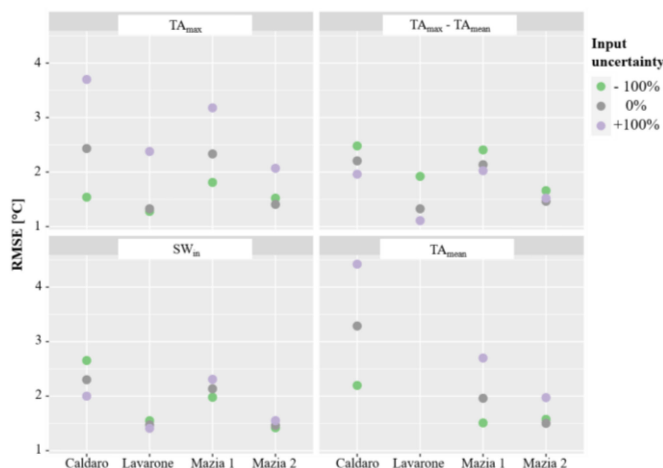

Fig. 12. RMSE values based on station-derived LST and predicted observations for two input scenarios: original variables (0%), and perturbated variables by $\pm100\%$ uncertainty values. For each model run only one predictor was changed.

ACKNOWLEDGMENT

REFERENCES

[1] M. C. Anderson, R. G. Allen, A. Morse, and W. P. Kustas, "Use of landsat thermal imagery in monitoring evapotranspiration and managing water resources," *Remote Sens. Environ.*, vol. 122, pp. 50–65, Jul. 2012.

[2] M. Castelli *et al.*, "Two-source energy balance modeling of evapotranspiration in alpine grasslands," *Remote Sens. Environ.*, vol. 209, pp. 327–342, May 2018.

[3] G. R. Diak *et al.*, "Estimating land surface energy budgets from space: Review and current efforts at the University of Wisconsin—Madison and USDA–ARS," *Bull. Amer. Meteorological Soc.*, vol. 85, no. 1, pp. 65–78, Jan. 2004.

[4] S. Leuzinger, R. Vogt, and C. Körner, "Tree surface temperature in an urban environment," *Agricultural Forest Meteorol.*, vol. 150, no. 1, pp. 56–62, Jan. 2010.

[5] I. Sandholt, K. Rasmussen, and J. Andersen, "A simple interpretation of the surface temperature/vegetation index space for assessment of surface moisture status," *Remote Sens. Environ.*, vol. 79, no. 2/3, pp. 213–224, Feb. 2002.

[6] D. A. Sims *et al.*, "A new model of gross primary productivity for north american ecosystems based solely on the enhanced vegetation index and land surface temperature from MODIS," *Remote Sens. Environ.*, vol. 112, no. 4, pp. 1633–1646, Apr. 2008.

[7] R. Huang, C. Zhang, J. Huang, D. Zhu, L. Wang, and J. Liu, "Mapping of daily mean air temperature in agricultural regions using daytime and nighttime land surface temperatures derived from TERRA and AQUA MODIS data," *Remote Sens.*, vol. 7, no. 7, pp. 8728–8756, Jul. 2015.

[8] N. Janatian *et al.*, "A statistical framework for estimating air temperature using MODIS land surface temperature data," *Int. J. Climatol.*, vol. 37, no. 3, pp. 1181–1194, May 2016.

[9] H. Meyer *et al.*, "Mapping daily air temperature for Antarctica based on MODIS LST," *Remote Sens.*, vol. 8, no. 9, Sep. 2016, Art. no. 732.

[10] Z. L. Li *et al.*, "Satellite-derived land surface temperature: Current status and perspectives," *Remote Sens. Environ.*, vol. 131, pp. 14–37, Apr. 2013.

[11] Z. Wan and J. Dozier, "A generalized split-window algorithm for retrieving land-surface temperature from space," *IEEE Trans. Geosci. Remote Sens.*, vol. 34, no. 4, pp. 892–905, Jul. 1996.

[12] F. B. Balçik, "Determining the impact of urban components on land surface temperature of Istanbul by using remote sensing indices," *Environ. Monit. Assessment*, vol. 186, pp. 859–872, Sep. 2013.

[13] K. Deilami and M. Kamruzzaman, "Modelling the urban heat island effect of smart growth policy scenarios in Brisbane," *Land Use Policy*, vol. 64, pp. 38–55, May 2017.

[14] D. Lu, K. Song, S. Zang, M. Jia, J. Du, and C. Ren, "The effect of urban expansion on urban surface temperature in Shenyang, China: An analysis with landsat imagery," *Environ. Model. Assessment*, vol. 20, pp. 197–210, Jun. 2015.

[15] J. A. Voogt and T. R. Oke, "Thermal remote sensing of urban climates," *Remote Sens. Environ.*, vol. 86, pp. 370–384, Aug. 2003.

[16] M. C. Anderson *et al.*, "The evaporative stress index as an indicator of agricultural drought in Brazil: An assessment based on crop yield impacts," *Remote Sens. Environ.*, vol. 174, pp. 82–99, Mar. 2016.

[17] S. Park, J. J. Feddema, and S. L. Egbert, "Impacts of hydrologic soil properties on drought detection with MODIS thermal data," *Remote Sens. Environ.*, vol. 89, pp. 53–62, Jan. 2004.

[18] S. Swain, B. D. Wardlow, S. Narumalani, T. Tadesse, and K. Callahan, "Assessment of vegetation response to drought in Nebraska using Terra-MODIS land surface temperature and normalized difference vegetation index," *GISci. Remote Sens.*, vol. 48, pp. 432–455, Jul. 2011.

[19] H. T. Tran, J. B. Campbell, T. D. Tran, and H. T. Tran, "Monitoring drought vulnerability using multispectral indices observed from sequential remote sensing (Case study: Tuy Phong, Binh Thuan, Vietnam)," *GISci. Remote Sens.*, vol. 54, no. 2, pp. 167–184, Mar. 2017.

[20] M. C. Anderson, C. Hain, B. Wardlow, A. Pimstein, J. R. Mecikalski, and W. P. Kustas, "Evaluation of drought indices based on thermal remote sensing of evapotranspiration over the continental United States," *J. Climate*, vol. 24, no. 8, pp. 2025–2044, Apr. 2011.

[21] S. Park, J. Im, E. Jang, and J. Rhee, "Drought assessment and monitoring through blending of multi-sensor indices using machine learning approaches for different climate regions," *Agricultural Forest Meteorol.*, vol. 216, pp. 157–169, Jan. 2016.

[22] M. C. Anderson, J. M. Norman, J. R. Mecikalski, J. A. Otkin, and W. P. Kustas, "A climatological study of evapotranspiration and moisture stress across the continental United States based on thermal remote sensing: 1. Model formulation," *J. Geophys. Res.-Atmos.*, vol. 112, May 2007, Art. no. D10.

[23] E. Carpintero *et al.*, "Continuous evapotranspiration monitoring and water stress at watershed scale in a Mediterranean Oak Savanna," in *Proc. Remote Sens. Agriculture, Ecosyst., Hydrol. XVIII. Int. Soc. Opt. Photon.*, Edinburgh, U.K., Oct. 2016, vol. 9998, Art. no. 99980N.

[24] S. Rahimi, M. A. Gholami Sefidkouhi, M. Raeini-Sarjaz, and M. Valipour, "Estimation of actual evapotranspiration by using MODIS images (a case study: Tajan catchment)," *Arch. Agronomy Soil Sci.*, vol. 61, no. 5, pp. 695–709, May 2015.

[25] R. Tang and Z. L. Li, "Evaluation of two end-member-based models for regional land surface evapotranspiration estimation from MODIS data," *Agricultural Forest Meteorol.*, vol. 202, pp. 69–82, Mar. 2015.

[26] T. Wang, J. Shi, H. Letu, Y. Ma, X. Li, and Y. Zheng, "Detection and removal of clouds and associated shadows in satellite imagery based on simulated radiance fields," *J. Geophys. Res. Atmos.*, vol. 124, no. 13, pp. 7207–7225, Jun. 2019.

[27] M. Jin, "Interpolation of surface radiative temperature measured from polar orbiting satellites to a diurnal cycle: 2. Cloudy-pixel treatment," *J. Geophys. Res. Atmos.*, vol. 105, no. D3, pp. 4061–4076, Feb. 2000.

[28] L. Lu, V. Venus, A. Skidmore, T. Wang, and G. Luo, "Estimating land-surface temperature under clouds using MSG/SEVIRI observations," *Int. J. Appl. Earth Observ. Geoinformat.*, vol. 13, no. 2, pp. 265–276, Apr. 2011.

[29] W. Yu, J. Tan, M. Ma, X. Li, X. She, and Z. Song, "An effective similar-pixel reconstruction of the high-frequency cloud-covered areas of Southwest China," *Remote Sens.*, vol. 11, no. 3, Jan. 2019, Art. no. 336.

[30] X. Zhang, J. Pang, and L. Li, "Estimation of land surface temperature under cloudy skies using combined diurnal solar radiation and surface temperature evolution," *Remote Sens.*, vol. 7, no. 1, pp. 905–921, Jan. 2015.

[31] C. Zeng, D. Long, H. Shen, P. Wu, Y. Cui, and Y. Hong, "A two-step framework for reconstructing remotely sensed land surface temperatures contaminated by cloud," *ISPRS J. Photogramm.*, vol. 141, pp. 30–45, Jul. 2018.

[32] G. Yang, W. Sun, H. Shen, X. Meng, and J. Li, "An integrated method for reconstructing daily MODIS land surface temperature data," *IEEE J. Sel. Topics Appl. Earth Observ. Remote Sens.*, vol. 12, no. 3, pp. 1026–1040, Mar. 2019.

[33] J. Martins *et al.*, "An all-weather land surface temperature product based on MSG/SEVIRI observations," *Remote Sens.*, vol. 11, no. 24, Jan. 2019, Art. no. 3044.

[34] P. Fu, Y. Xie, Q. Weng, S. Myint, K. Meacham-Hensold, and C. Bernacchi, "A physical model-based method for retrieving urban land surface temperatures under cloudy conditions," *Remote Sens. Environ.*, vol. 230, Sep. 2019, Art. no. 111191.

[35] H. Gao, R. Fu, R. E. Dickinson, and R. I. N. Juárez, "A practical method for retrieving land surface temperature from AMSR-E over the amazon forest," *IEEE Trans. Geosci. Remote Sens.*, vol. 46, no. 1, pp. 193–199, Dec. 2007.

[36] H. R. Shwetha and D. N. Kumar, "Prediction of high spatio-temporal resolution land surface temperature under cloudy conditions using microwave vegetation index and ANN," *ISPRS J. Photogramm.*, vol. 117, pp. 40–55, Jul. 2016.

[37] S. B. Duan, Z. L. Li, and P. Leng, "A framework for the retrieval of all-weather land surface temperature at a high spatial resolution from polar-orbiting thermal infrared and passive microwave data," *Remote Sens. Environ.*, vol. 195, pp. 107–117, Jun. 2017.

[38] W. Tang, D. Xue, Z. Long, X. Zhang, and J. Zhou, "Near-real-time estimation of 1-km all-weather land surface temperature by integrating satellite passive microwave and thermal infrared observations," *IEEE Geosci. Remote Sens. Lett.*, vol. 19, pp. 1–5, Apr. 2021, Art. no. 7001305.

[39] X. Zhang, J. Zhou, S. Liang, L. Chai, D. Wang, and J. Liu, "Estimation of 1-km all-weather remotely sensed land surface temperature based on reconstructed spatial-seamless satellite passive microwave brightness temperature and thermal infrared data," *ISPRS J. Photogramm.*, vol. 167, pp. 321–344, Sep. 2020.

[40] D. Long *et al.*, "Generation of MODIS-like land surface temperatures under all-weather conditions based on a data fusion approach," *Remote Sens. Environ.*, vol. 246, Sep. 2020, Art. no. 111863.

[41] C. M. Frey and C. Künzer, "Land surface temperature dynamics in the Upper Mekong Basin derived from MODIS time series," *Int. J. Remote Sens.*, vol. 35, no. 8, pp. 2780–2798, Apr. 2014.

[42] M. Neteler, "Estimating daily land surface temperatures in mountainous environments by reconstructed MODIS LST data," *Remote Sens.*, vol. 2, no. 1, pp. 333–351, Jan. 2010.

[43] M. Sarafanov, E. Kazakov, N. O. Nikitin, and A. V. Kalyuzhnaya, "A machine learning approach for remote sensing data gap-filling with open-source implementation: An example regarding land surface temperature, surface Albedo and NDVI," *Remote Sens.*, vol. 12, no. 23, Nov. 2020, Art. no. 3865.

[44] D. J. Weiss, P. M. Atkinson, S. Bhatt, B. Mappin, S. I. Hay, and P. W. Gething, "An effective approach for gap-filling continental scale remotely sensed time-series," *ISPRS J. Photogramm.*, vol. 98, pp. 106–118, Dec. 2014.

[45] Y. Xu and Y. Shen, "Reconstruction of the land surface temperature time series using harmonic analysis," *Comput. Geosci.*, vol. 61, pp. 126–132, Dec. 2013.

[46] W. L. Crosson, M. Z. Al-Hamdan, S. N. Hemmings, and G. M. Wade, "A daily merged MODIS aqua–terra land surface temperature data set for the conterminous United States," *Remote Sens. Environ.*, vol. 119, pp. 315–324, Apr. 2012.

[47] T. Wang *et al.*, "Recovering land surface temperature under cloudy skies considering the solar-cloud-satellite geometry: Application to MODIS and landsat-8 data," *J. Geophys. Res. Atmos.*, vol. 124, no. 6, pp. 3401–3416, Mar. 2019.

[48] L. Ke, X. Ding, and C. Song, "Reconstruction of time-series MODIS LST in Central Qinghai-Tibet Plateau using geostatistical approach," *IEEE Geosci. Remote Sens. Lett.*, vol. 10, no. 6, pp. 1602–1606, Jun. 2013.

[49] X. M. Fan, H. G. Liu, G. H. Liu, and S. B. Li, "Reconstruction of MODIS land-surface temperature in a flat terrain and fragmented landscape," *Int. J. Remote Sens.*, vol. 35, no. 23, pp. 7857–7877, Dec. 2014.

[50] P. Wu, Z. Yin, H. Yang, Y. Wu, and X. Ma, "Reconstructing geostationary satellite land surface temperature imagery based on a multiscale feature connected convolutional neural network," *Remote Sens,* vol. 11, no. 3, Jan. 2019, Art. no. 300.

[51] W. Zhao and S. B. Duan, "Reconstruction of daytime land surface temperatures under cloud-covered conditions using integrated MODIS/Terra land products and MSG geostationary satellite data," *Remote Sens. Environ.*, vol. 247, Sep. 2020, Art. no. 11931.

[52] P. Bartkowiak, M. Castelli, and C. Notarnicola, "Downscaling land surface temperature from MODIS dataset with random forest approach over alpine vegetated areas," *Remote Sens,* vol. 11, no. 11, Jun. 2019, Art. no. 1319.

[53] G. Bertoldi, S. D. Chiesa, C. Notarnicola, L. Pasolli, G. Niedrist, and U. Tappeiner, "Estimation of soil moisture patterns in mountain grasslands by means of SAR RADARSAT2 images and hydrological modeling," *J. Hydrol.*, vol. 516, pp. 245–257, Aug. 2014.

[54] G. Pastorello *et al.*, "The FLUXNET2015 dataset and the ONEFlux processing pipeline for eddy covariance data," *Sci. Data.,* vol. 7, no. 1, pp. 1–27, Jul. 2020.

[55] A. K. Heidinger, I. Laszlo, C. C. Molling, and D. Tarpley, "Using SURFRAD to verify the NOAA single-channel land surface temperature algorithm," *J. Atmos. Ocean. Technol.*, vol. 30, no. 12, pp. 2868–2884, Dec. 2013.

[56] Z. Xing *et al.*, "Estimation of daily mean land surface temperature at global scale using pairs of daytime and nighttime MODIS instantaneous observations," *ISPRS J. Photogramm.*, vol. 178, pp. 51–67, Aug. 2021.

[57] G. Hulley, N. Malakar, and R. Freepartner, "Moderate resolution imaging spectroradiometer (MODIS) land surface temperature and emissivity product (MxD21) algorithm theoretical basis document collection-6," Pasadena, California, USA: JPL Publication, Dec. 2016, pp. 12–17.

[58] K. Wang *et al.*, "Estimation of surface long wave radiation and broadband emissivity using moderate resolution imaging spectroradiometer (MODIS) land surface temperature/emissivity products," *J. Geophys. Res. Atmospheres*, vol. 110, Jun. 2005, Art. no. D11.

[59] G. Hulley and J. Nickeson, "M*D21 (MYD21/MOD21) and M*D11 (MYD11/MYD21) land surface temperature and emissivity (LST&E) products status report," Aug. 2020.

[60] K. Gallo, R. Hale, D. Tarpley, and Y. Yu, "Evaluation of the relationship between air and land surface temperature under clear-and cloudy-sky conditions," *J. Appl. Meteorol. Climatol.*, vol. 50, no. 3, pp. 767–775, Mar. 2011.

[61] D. J. Mildrexler, M. Zhao, and S. W. Running, "A global comparison between station air temperatures and MODIS land surface temperatures reveals the cooling role of forests," *J. Geophys. Res. BioGeosci.*, vol. 116, Sep. 2011, Art. no. G3.

[62] J. Silva, C. Ribeiro, and R. Guedes, "Roughness length classification of corine land cover classes," in *Proc. Eur. Wind Energy Conf.*, Milan, Italy, vol. 710, May 2007, Art. no. 110.

[63] J. Cho, S. Miyazaki, P. J. F. Yeh, W. Kim, S. Kanae, and T. Oki, "Testing the hypothesis on the relationship between aerodynamic roughness length and albedo using vegetation structure parameters," *Int. J. Biometeorol.*, vol. 56, no. 2, pp. 411–418, May 2012.

[64] L. Laiti *et al.*, "A solar atlas for the trentino region in the Alps: Quality control of surface radiation data," *Energy Procedia*, vol. 59, pp. 336–343, Jan. 2014.

[65] A. Crespi, M. Matiu, G. Bertoldi, M. Petitta, and M. Zebisch, "A high-resolution gridded dataset of daily temperature and precipitation records (1980–2018) for trentino–South Tyrol (North-Eastern Italian Alps)," *Earth Syst. Sci. Data Discuss.*, vol. 13, no. 6, pp. 2801–2818, Jun. 2021.

[66] M. New, M. Hulme, and P. Jones, "Representing twentieth-century space–time climate variability. Part II: Development of 1901–96 monthly grids of terrestrial surface climate," *J. Clim.*, vol. 13, no. 13, pp. 2217–2238, Jul. 2000.

[67] C. Schaaf and Z. Wang, "MCD43A3 MODIS/Terra+Aqua BRDF/Albedo daily L3 Global − 500m V006," NASA EOS-DIS Land Processes DAAC, NASA, WA, DC, USA, 2015, doi: 10.5067/MODIS/MCD43A3.

[68] B. J. Choudhury and J. L. Monteith, "A four-layer model for the heat budget of homogeneous land surfaces," *Quart. J. Roy. Meteorological Soc.*, vol. 114, no. 480, pp. 373–398, Jan. 1988.

[69] K. J. Schaudt and R. E. Dickinson, "An approach to deriving roughness length and zero-plane displacement height from satellite data, prototyped with BOREAS data," *Agricultural Forest Meteorol.*, vol. 104, no. 2, pp. 143–155, Aug. 2000.

[70] R. Myneni, Y. Knyazikhin, and T. Park, "MCD15A3H MODIS/Terra+Aqua leaf area Index/FPAR 4-day L4 Global 500m SIN grid V006," NASA EOSDIS Land Processes DAAC, NASA, WA, DC, USA, 2015, doi: 10.5067/MODIS/MCD15A3H.

[71] Z. Wan, S. Hook, and G. Hulley, "MOD11A1 MODIS/Terra land surface temperature/emissivity daily L3 global 1km SIN grid V006," NASA EOSDIS Land Processes DAAC, NASA, WA, DC, USA, 2015, doi: 10.5067/MODIS/MOD11A1.

[72] K. Didan, "MOD13Q1 MODIS/Terra vegetation indices 16-Day L3 global 250m SIN grid V006," NASA EOSDIS Land Processes DAAC, NASA, WA, DC, USA, 2015, doi: 10.5067/MODIS/MOD13Q1.

[73] LISS, "LISS-2013 – Land Use Information in South Tyrol: Update Harmonization with European Standards and Integration of Research Results," Autonome Provinz Bozen/Provincia autonoma di Bolzano, 28.0.1 Landeskartographie und Koordination der Geodaten, 2013.

[74] C. Notarnicola *et al.*, "Snow cover maps from MODIS images at 250 m resolution, Part 1: Algorithm description," *Remote Sens.*, vol. 5, no. 1, pp. 110–126, Jan. 2013.

[75] R. Lecerf, L. Hubert-Moy, T. Corpetti, F. Baret, B. A. Latif, and H. Nicolas, "Estimating biophysical variables at 250 m with reconstructed EOS/MODIS time series to monitor fragmented landscapes," in *Proc. IEEE Int. Geosci. Remote Sens. Symp.*, Boston, MA, USA, vol. 2, pp. II–954, Jul. 2008.

[76] M. Machwitz, U. Gessner, C. Conrad, U. Falk, J. Richters, and S. Dech, "Modelling the gross primary productivity of west Africa with the regional biomass model RBM+, using optimized 250 m MODIS FPAR and fractional vegetation cover information," *Int. J. Appl. Earth Obs.*, vol. 43, pp. 177–194, Dec. 2015.

[77] M. Matiu, A. Jacob, and C. Notarnicola, "Daily MODIS snow cover maps for the European Alps from 2002 onwards at 250 m horizontal resolution along with a nearly cloud-free version," *Data*, vol. 5, no. 1, Mar. 2020.

[78] F. Zambrano, M. Lillo-Saavedra, K. Verbist, and O. Lagos, "Sixteen years of agricultural drought assessment of the Biobío region in Chile using a 250 m resolution vegetation condition index (VCI)," *Remote Sens.*, vol. 8, no. 6, Jun. 2016, Art. no. 530.

[79] A. Ignatov and G. Gutman, "Monthly mean diurnal cycles in surface temperatures over land for global climate studies," *J. Climate*, vol. 12, no. 7, pp. 1900–1910, Jul. 1999.

[80] N. A. Engerer and F. P. Mills, "Validating nine clear sky radiation models in Australia," *Sol. Energy*, vol. 120, pp. 9–24, Oct. 2015.

[81] J. Remund, L. Wald, M. Lefèvre, T. Ranchin, and J. Page, "Worldwide Linke turbidity information," in *Proc. Sol. World Congr. Int. Sol. Energy Soc.*, Göteborg, Sweden, vol. 400, Jun. 16, 2003, Art. no. 13.

[82] C. Rigollier, O. Bauer, and L. Wald, "On the clear sky model of the ESRA—European solar radiation Atlas—With respect to the heliosat method," *Sol. Energy*, vol. 68, no. 1, pp. 33–48, Jan. 2000.

[83] A. Benali, A. C. Carvalho, J. P. Nunes, N. Carvalhais, and A. Santos, "Estimating air surface temperature in Portugal using MODIS LST data," *Remote Sens. Environ.*, vol. 124, pp. 108–121, Sep. 2012.

[84] D. Y. Kim and K. S. Han, "Remotely sensed retrieval of midday air temperature considering atmospheric and surface moisture conditions," *Int. J. Remote Sens.*, vol. 34, no. 1, pp. 247–263, Jan. 2013.

[85] L. Breiman, "Random forests," *Mach. Learn.*, vol. 45, pp. 5–32, Oct. 2001.

[86] M. Kuhn and K. Johnson, *Applied Predictive Modeling*, vol. 26, 1st ed. New York, NY, USA: Springer, 2013, pp. 13–203.

[87] B. D. Ripley, *Pattern Recognition and Neural Networks*. Cambridge, U.K.: Cambridge Univ. Press, 2007.

[88] M. Fernández-Delgado, E. Cernadas, S. Barro, and D. Amorim, "Do we need hundreds of classifiers to solve real world classification problems?," *J. Mach. Learn. Res.*, vol. 15, no. 1, pp. 3133–3181, Jan. 2014.

[89] S. Talukdar, P. Singha, S. Mahato, S. Pal, Y. A. Liou, and A. Rahman, "Land-use land-cover classification by machine learning classifiers for satellite observations—A review," *Remote Sens,* vol. 12, no. 7, Jan. 2020, Art. no. 1135.

[90] H. Meyer and E. Pebesma, "Predicting into unknown space? Estimating the area of applicability of spatial prediction models," *Methods Ecol. Evol.*, vol. 12, pp. 1620–1633, Jun. 2021.

[91] J. F. Hair *et al.*, *Multivariate Data Analysis: A Global Perspective*, 7th ed. Upper Saddle River, NJ, USA: Prentice-Hall, 2009.

[92] H. Meyer, C. Reudenbach, S. Wöllauer, and T. Nauss, "Importance of spatial predictor variable selection in machine learning applications–Moving from data reproduction to spatial prediction," *Ecol. Model.*, vol. 411, Nov. 2019, Art. no. 108815.

[93] H. Meyer, C. Reudenbach, T. Hengl, M. Katurji, and T. Nauss, "Improving performance of spatio-temporal machine learning models using forward feature selection and target-oriented validation," *Environ. Model. Softw.*, vol. 101, pp. 1–9, Mar. 2018.

[94] D. R. Roberts *et al.*, "Cross-validation strategies for data with temporal, spatial, hierarchical, or phylogenetic structure," *Ecography*, vol. 40, no. 8, pp. 913–929, Aug. 2017.

[95] P. Schratz, J. Muenchow, E. Iturritxa, J. Richter, and A. Brenning, "Hyperparameter tuning and performance assessment of statistical and machine-learning algorithms using spatial data," *Ecol. Model.*, vol. 406, pp. 109–120, Aug. 2019.

[96] M. Kuhn, "Building predictive models in R using the caret package," *J. Stat. Softw.*, vol. 28, no. 5, pp. 1–26, Nov. 2008.

[97] M. Kuhn, "The caret package," *J. Stat. Softw.*, vol. 28, Nov. 2009, Art. no. 5.

[98] H. Meyer, C. Reudenbach, M. Ludwig, T. Nauss, and M. H. Meyer, "Package 'CAST'," *R package version 0.5.1*, Apr. 2021.

[99] R. C. Team, "R: A language and environment for statistical computing," *R Found. Statist. Comput.*, Vienna, Austria, 2013.

[100] N. Bystriakova, M. Peregrym, R. H. Erkens, O. Bezsmertna, and H. Schneider, "Sampling bias in geographic and environmental space and its effect on the predictive power of species distribution models," *Syst. Biodiversity*, vol. 10, no. 3, pp. 305–315, Aug. 2012.

[101] R. Kadmon, O. Farber, and A. Danin, "Effect of roadside bias on the accuracy of predictive maps produced by bioclimatic models," *Ecological Appl.*, vol. 14, no. 2, pp. 401–413, Apr. 2004.

[102] M. Jin and R. E. Dickinson, "Land surface skin temperature climatology: Benefitting from the strengths of satellite observations," *Environ. Res. Lett.*, vol. 5, no. 4, Nov. 2010, Art. no. 044004.

[103] P. A. Schultz and M. S. Halpert, "Global analysis of the relationships among a vegetation index, precipitation and land surface temperature," *Remote Sens.*, vol. 16, no. 15, pp. 2755–2777, Oct. 1995.

[104] L. Busetto, M. Meroni, and R. Colombo, "Combining medium and coarse spatial resolution satellite data to improve the estimation of sub-pixel NDVI time series," *Remote Sens. Environ.*, vol. 112, no. 1, pp. 118–131, Jan. 2008.

[105] F. Gao, J. Masek, M. Schwaller, and F. Hall, "On the blending of the landsat and MODIS surface reflectance: Predicting daily landsat surface reflectance," *IEEE Trans. Geosci. Remote Sens.*, vol. 44, no. 8, pp. 2207–2218, Aug. 2006.

[106] P. D'odorico, Y. He, S. Collins, S. F. De Wekker, V. Engel, and J. D. Fuentes, "Vegetation–microclimate feedbacks in woodland–grassland ecotones," *Glob. Ecol. Biogeography,* vol. 22, no. 4, pp. 364–379, Apr. 2013.

[107] L. Congedo, L. Sallustio, M. Munafò, M. Ottaviano, D. Tonti, and M. Marchetti, "Copernicus high-resolution layers for land cover classification in Italy," *J. Maps*, vol. 12, no. 5, pp. 1195–1205, Feb. 2016.

[108] N. P. Majozi, C. M. Mannaerts, A. Ramoelo, R. Mathieu, and W. Verhoef, "Uncertainty and sensitivity analysis of a remote-sensing-based penman–Monteith model to meteorological and land surface input variables," *Remote Sens.*, vol. 13, no. 5, Feb. 2021, Art. no. 882.

[109] L. Sun *et al.*, "Reconstructing daily clear-sky land surface temperature for cloudy regions from MODIS data," *Comput. Geosci.*, vol. 105, pp. 10–20, Aug. 2017.

[110] K. Makowski, E. B. Jaeger, M. Chiacchio, M. Wild, T. Ewen, and A. Ohmura, "On the relationship between diurnal temperature range and surface solar radiation in Europe," *J. Geophys. Res. Atmos.*, vol. 114, Apr. 2009, Art. no. D10.

[111] X. Li, Y. Zhou, G. R. Asrar, and Z. Zhu, "Creating a seamless 1 km resolution daily land surface temperature dataset for urban and surrounding areas in the conterminous United States," *Remote Sens. Environ.*, vol. 206, pp. 84–97, Mar. 2018.

[112] W. Yu, M. Ma, X. Wang, and J. Tan, "Estimating the land-surface temperature of pixels covered by clouds in MODIS products," *J. Appl. Remote Sens.*, vol. 8, no. 1, Nov. 2014, Art. no. 083525.

[113] B. Jiang, S. Liang, J. Wang, and Z. Xiao, "Modeling MODIS LAI time series using three statistical methods," *Remote Sens. Environ.*, vol. 114, no. 7, pp. 1432–1444, Jul. 2010.

[114] E. G. Moody, M. D. King, S. Platnick, C. B. Schaaf, and F. Gao, "Spatially complete global spectral surface Albedos: Value-added datasets derived from Terra MODIS land products," *IEEE Trans. Geosci. Remote Sens.*, vol. 43, no. 1, pp. 144–158, Jan. 2005.

[115] L. Pasolli *et al.*, "Retrieval of leaf area index in mountain grasslands in the Alps from MODIS satellite imagery," *Remote Sens. Environ.*, vol. 165, pp. 159–174, Aug. 2015.

[116] M. Reichstein, G. Camps-Valls, B. Stevens, M. Jung, J. Denzler, and N. Carvalhais, "Deep learning and process understanding for data-driven Earth system science," *Nature*, vol. 566, no. 7743, pp. 195–204, Feb. 2019.

[117] W. P. Tsai, M. Pan, K. Lawson, J. Liu, D. Feng, and C. Shen, "From parameter calibration to parameter learning: Revolutionizing large-scale geoscientific modeling with big data," in *AGU Fall Meeting Abstr.*, vol. 20, pp. H166–0016, Dec. 2020.

[118] S. See and J. Adie, "Challenges and opportunities for a hybrid modelling approach to earth system science," in *Proc. CCF THPC*, Jul. 2021, pp. 1–10.

[119] J. Willard, X. Jia, S. Xu, M. Steinbach, and V. Kumar, "Integrating physics-based modeling with machine learning: A survey," Jul. 2021, *arXiv:2003.04919*.

[120] H. R. Ghafarian Malamiri, I. Rousta, H. Olafsson, H. Zare, and H. Zhang, "Gap-filling of MODIS time series land surface temperature (LST) products using singular spectrum analysis (SSA)," *Atmosphere*, vol. 9, no. 9, Aug. 2018, Art. no. 334.

[121] M. Metz, D. Rocchini, and M. Neteler, "Surface temperatures at the continental scale: Tracking changes with remote sensing at unprecedented detail," *Remote Sens.*, vol. 6, no. 5, pp. 3822–3840, Apr. 2014.

Paulina Bartkowiak (Student Member, IEEE) received the B.Sc. degree in geodesy and cartography and the M.Sc. in geodesy and cartography from the Warsaw University of Technology, Warsaw, Poland, in 2014 and 2016, respectively. She is currently working toward the Doctoral degree in environmental science with the Department of Earth and Environmental Sciences, University of Milano-Bicocca, Milan, Italy, and with the Institute for Earth Observation, Eurac Research, Bolzano, Italy.

Her thesis is focused on development of a new satellite-based land surface temperature product for further evapotranspiration modeling in the Alps. Her research interests include optical and thermal remote sensing with main focus on image processing and machine learning.

Ms. Bartkowiak was the recipient of the REACH Prize for Ph.D. research funded by the European Space Agency and SpaceBrains Foundation, in 2020.

Mariapina Castelli received the master's degree in environmental engineering from the University of Perugia in 2009, and the Ph.D degree in environmental engineering from the University of Trento, Trento, Italy, in 2015.

She is currently a Senior Researcher with the Eurac Institute for Earth Observation. Her main research interests include developing methods to support water resources management by using satellite data in water and energy balance models, focusing on defining proper processing lines to deal with the topographic complexity and land-cover heterogeneity of mountainous regions. Her current research interests include estimating evapotranspiration based by energy balance models, studying the impact of climate change on the water cycle, and developing innovative solutions to support drought risk management for mountain agriculture based on satellite data.

Alice Crespi received the M.Sc and Ph.D. degrees in physics from the University of Milan, Milan, Italy, in 2015 and 2018, respectively.

She is currently a Postdoc Researcher with the Institute for Earth Observation of Eurac Research. Her research is focused on the analysis of climate and meteorological data for the assessment of the spatio-temporal variability and trends of the climate signal, with a particular attention to climate extremes, and on the provision of effective climate data and tools supporting the risk assessment in mountain regions, which includes the implementation of interpolation techniques modeling the influence of orography on the spatial distribution of meteorological variables and the definition of proper postprocessing statistical approaches to derive climate model simulations at the local scale.

Georg Niedrist received the master's degree in ecology from the University of Innsbruck, Innsbruck, Austria, in 2006, and the Ph.D. degree in ecology from the Colorado State University, Fort Collins, CO, USA, in 2016.

In 2006, he joined Eurac Research. Beside "standard" research activities, he is technical coordinator of the LTER site Matsch/Mazia and Codeveloper of the terraXcube, a special research facility to study climate change effects on high alpine ecosystems. His research interests include mountain agriculture, biodiversity, and climate change.

Damiano Zanotelli received the joint Ph.D. degree in horticultural sciences from the Universities of Bologna and Bolzano, Bolzano, Italy, in 2012.

He is currently an Assistant Professor (tenure track RTD/B) with the Faculty of Science and Technology, Free University of Bozen-Bolzano, Bolzano, Italy. His main research interests include the assessment of carbon and water fluxes in the soil–plant–atmosphere continuum of woody agroecosystems in standard and stressed conditions.

Dr. Zanotelli was the recipient of Best Jung Researcher for the category "Fruticulture" by the Italian Society of Horticultural Sciences in September 2016.

Roberto Colombo received the master's degree in earth science from the University of Milan, Milan, Italy, in 1991.

He wrote his thesis on the use of remotely sensed data for geomorphological mapping of the inland delta of the Niger River in Mali. Roberto Colombo is professor of Remote Sensing at the Department of Environmental Sciences, University of Milano-Bicocca. His research interest is to develop remote sensing tools for quantitative estimation of land surface properties. He works with a wide range of Earth Observation data at different scales and geophysical methods, assimilating multi-source, multi-spectral and multi-temporal remote sensing data, from field spectroscopy to satellite level for modelling terrestrial and environmental dynamics, with focus on vegetation fluorescence and snow properties. Current activities include space mission concepts and definition, airborne campaigns and field cal/val strategies, engineering and design of proximal remote sensing instruments, algorithm development, environmental modelling and new applications.

Claudia Notarnicola (Member, IEEE) received the M.S. (*summa cum laude*) and the Ph.D. degrees in physics from the University of Bari, Bari, Italy, in 1995 and 2002, respectively.

She is currently the Vice-Head of the Institute for Earth Observation, Eurac Research, Bolzano, Italy, where she is also the Leader of a group dealing with remote sensing applications in the synthetic aperture radar (SAR) and optical domain for soil, snow, and vegetation monitoring, as well as integration of remotely sensed observations with models and ground measurements. She conducts research within the frameworks of several national and international projects. Among others, she was also involved in the Cassini - Huygens Mission for the application of an inversion procedure to the estimation of Titan surface parameters. Her research interests include biophysical parameter (soil moisture, vegetation, and snow) retrieval using optical and SAR images, optical and SAR data processing, data fusion, and electromagnetic models.

Dr. Notarnicola has been a Conference Chair for the SPIE International Conference on Active and Passive Microwave Remote Sensing for Environmental Monitoring since 2006. She was recipient of the South Tyrol Women in Science Award in 2020.